SYMPTOMS OF ANTIMICROBIAL PEPTIDE STRESS: THE ATTACK OF LL-37 AND ALAMETHICIN ON THE MODEL ORGANISM *BACILLUS SUBTILIS*

By

Kenneth J. Barns

A dissertation submitted in partial fulfillment of

The requirements for the degree of

Doctor of Philosophy

(Chemistry)

at the

THE UNIVERSITY OF WISCONSIN-MADISON

2014

Date of final oral examination: 6/11/2014

The dissertation is approved by the following members of the Final Oral Committee:

James C. Weisshaar, Professor, Chemistry

Samuel H. Gellman, Professor, Chemistry

M. Thomas Record, Professor, Chemistry and Biochemistry

Randall Goldsmith, Assistant Professor, Chemistry

Jade Wang, Associate Professor, Bacteriology

To Mom and Dad, who will smile and nod during my Thesis Defense ☺

Acknowledgements

I'd like to thank the people who guided me through chemistry in high school and at my undergraduate institution, including Mr. Probst, Mr. Brandt, Dr. Kathy Severin, Dr. Kevin Dillman, Dr. Sanela Lampa-Pastirk, and Professor Warren F. Beck. Your teaching and guidance led me to pursue a graduate degree in chemistry.

I thank Weisshaar group members, past and present. I thank Dr. Kem Sochacki for starting me on the antimicrobial peptide project and directing me through my early, rocky years as a graduate student. I thank Dr. Benjamin Bratton and Dr. Colin Ingram for their guidance and training. Dr. Renee Dalrymple for her conversation and advice. Dr. Somenath Bakshi for his scientific insight throughout my PhD career; I always believed I was very lucky that I joined the same group as a scientist whom I respect so much. I thank past and present Weisshaar group members Dr. Izzy Smith, Dr. TingTing Wang, Heejun Choi, Nambirajan Rangarajan, Wenting Li, Sonisilpa Mohapatra, Nikolai Radzinski, and Zhilin Yang.

I thank my committee, as well as my advisor Professor James Weisshaar. I enjoyed our scientific talks, and look forward to reading the subsequent papers from your group.

Lastly, I thank my family and friends, including my parents Gail and Wilson Barns, my brothers Jeff and Doug, and my Aunt Marie, Uncle Bob, and my cousin Rob. Thank you to all of the graduate students I met during my time here; you kept me sane ☺.

SYMPTOMS OF ANTIMICROBIAL PEPTIDE STRESS: THE ATTACK OF LL-37 AND ALAMETHICIN ON THE MODEL ORGANISM *BACILLUS SUBTILIS*

Under the supervision of Professor James C. Weisshaar

At the University of Wisconsin-Madison

Abstract

Antimicrobial peptides are a class of compounds with broad-spectrum antibacterial activity, found in several different species. While there has been considerable research on these peptides, both on live bacteria and on model lipid bilayers, the details of their mechanism of action is still a mystery. We present time-lapse, single cell fluorescence microscopy data on the model Gram-positive bacterium *Bacillus subtilis* exposed to the antimicrobial peptides LL-37 and alamethicin. Our technique allows simultaneous measurement of cell growth, cell envelope permeability, and the pH component of the proton motive force on individual cells. Exposure to either LL-37 or alamethicin leads to the permeabilization of the cytoplasmic membrane, which occurs simultaneously with nucleoid staining by Sytox Green/Orange, and abrupt cell shrinkage. The cells become permeable to larger species like GFP at longer times of exposure, and eventually lyse. While both peptides show similarities, important differences are seen by comparing the staining dynamics of the DNA stains Sytox Green/Orange. LL-37 shows evidence for localized membrane permeabilization, while alamethicin does not. Our data sheds light on the exact symptoms and mechanisms of antimicrobial stress.

Here is a list of the papers I wrote on my dissertation work.

1. Barns, K.J. and J. C. Weisshaar. 2013.Real-Time attack of LL-37 on single *Bacillus subtilis* cells. Biochimica et Biophysica Acta. 1828:1511-1520.

2. Barns, K.J. and J. C. Weisshaar. 2014. Non-localized membrane distruption in *Bacillus subtilis* caused by Alamethicin. (In Preparation)

TABLE OF CONTENTS

Contents

Chapter 1

Introduction

The 20th century saw a dramatic decrease in the death of United States citizens from infectious diseases. The Center for Disease Control attributes this decrease to improvements in sanitation, hygiene, and disease prevention, vaccinations, and antibiotics.[1] Antibiotics have been used commercially since the 1940's to treat infections caused by bacteria ranging from *Streptococcus pneumonia* and *Staphylococcus aureus* (both gram-positive), to *Escherichia coli* and *Pseudomonas aeruginosa* (both gram-negative), to *Mycobacterium tuberculosis*. In the early days of their use, it was startling to see how patients who were at death's door could be saved by these drugs (often termed "magic bullets"). The history of antibiotics tends to focus on their discovery, as well as the constant battle between bacterial resistance and new antibiotics. To introduce my research, I will focus on a different story: the history of the research devoted to *understanding* how these "magic bullets" kill and/or inhibit bacteria.

To illustrate my point, I will give a brief history of penicillin, focusing on the research devoted to understanding how it kills or inhibits bacteria (its "mechanism of action"). Penicillin was first discovered by Alexander Fleming in 1928.[2, 3] After overcoming difficulties in purifying penicillin, by 1944, penicillin was being produced in mass quantities, and used to treat wounds in infected soldiers during World War II. Alexander Fleming, Howard Florey, and Ernst Chain were awarded the Nobel Prize in

Physiology or Medicine in 1945, "*For the discovery of penicillin and its curative effect in various infectious diseases.*" The discovery of penicillin to its common use as a treatment for infectious disease spanned less than 20 years. What about the research on its mechanism of action?

Penicillin was found to bind to specific proteins (named penicillin binding proteins, or PBP's) involved in the synthesis of the peptidoglycan (PG) layer. One of the early models of penicillin's mechanism of action from 1965 suggested that the inactivation of the PBP's leads to a compromised PG layer unable to contain the pressure differential (turgor pressure) between the cytoplasm and the extracellular medium. [4] Once the PG layer was weak enough, the cells would rupture (lysis). However, researchers in the 1960's found that some of the cell's own enzymes, called autolysins, were actively degrading the PG layer; cells without these enzymes showed an increased resistance to penicillin. [5] In 1990, researchers found that suppression of autolysins gave *Streptococcus pneumonia* only partial protection from penicillin. They proposed an autolysin-independent mechanism of killing that worked at a slower rate than autolysin-dependent cell lysis. [6] Even by the turn of the century, the details of penicillin's bactericidal action was still an active area of research. [7, 8]

Researchers were still elucidating the details of penicillin's mechanism of action 50 years after its introduction into medicine, and 70 years after its discovery. Penicillin is not alone; other "classical" antibiotics, such as kanamycin, still have mysteries associated with their mechanism of action. [9] *Our understanding of the bactericidal/bacteriostatic action of antibiotics lags far behind our usage of them in medicine*. In a time of increased resistance to classical antibiotics, understanding the mechanism by which antimicrobial compounds kill or inhibit bacteria could help us in the development of new "magic bullets."

Our research aims to fill in the gaps of knowledge associated with a more recently discovered group of compounds, antimicrobial peptides (AMP's). Our methods utilize time-lapse, single cell

fluorescence microscopy to observe the effects of antimicrobial stress in real time. We will begin by reviewing the cell structure of our model bacterium, *Bacillus subtilis*. We then describe the fundamentals of antimicrobial peptides, as well as details of our experimental methods. The thesis concludes with results from two antimicrobial peptides; the human cathelicidin LL-37, and the fungal peptaibol alamethicin.

Cell Envelope of Bacillus subtilis

Bacillus subtilis has been used as a model Gram-positive bacterium for decades. While there are no strains of *B. subtilis* that are pathogenic to humans, *B. subtilis* exists, and can grow, in the digestive track of several mammals, indicating it may come into contact with antimicrobial peptides during its normal life cycle. [10, 11] Since the antimicrobial peptides of interest interact with lipid membranes [12, 13], we begin by reviewing the cell envelope structure of bacteria. Figure 1.1 shows the differences in cell envelope structure between a Gram-negative bacterium (such as *Escherichia coli*), and a Gram-positive bacterium (such as *Bacillus subtilis*). It is important to remember that the differences between Gram-negative and Gram-positive bacteria go much further than cell envelope alone, but Fig. 1.1 provides a starting point in discussing the differences and similarities. This thesis focuses on *B. subtilis* (strain 168), so more explanation will be devoted to its cell envelope structure.

Both Gram-negative and -positive bacteria have a lipid membrane (cytoplasmic membrane, CM) to separate the inside of the cell from the extracellular medium. Both bacteria have a peptidoglycan layer that defines the shape of the cell. The cytoplasm of bacteria is highly concentrated in solutes and biomolecules, which causes an osmotic pressure (called turgor pressure) between the cytoplasm and the extracellular medium. The PG layer resists this turgor pressure, and keeps the cell from rupturing. The PG layer for Gram-positive organisms is thicker than that of Gram-negative organisms. The turgor

pressure for *B. subtilis* has been estimated to be ~1.9 MPa [14], while a Gram-negative bacterium like *E. coli* has a turgor pressure less than a tenth value. [15]

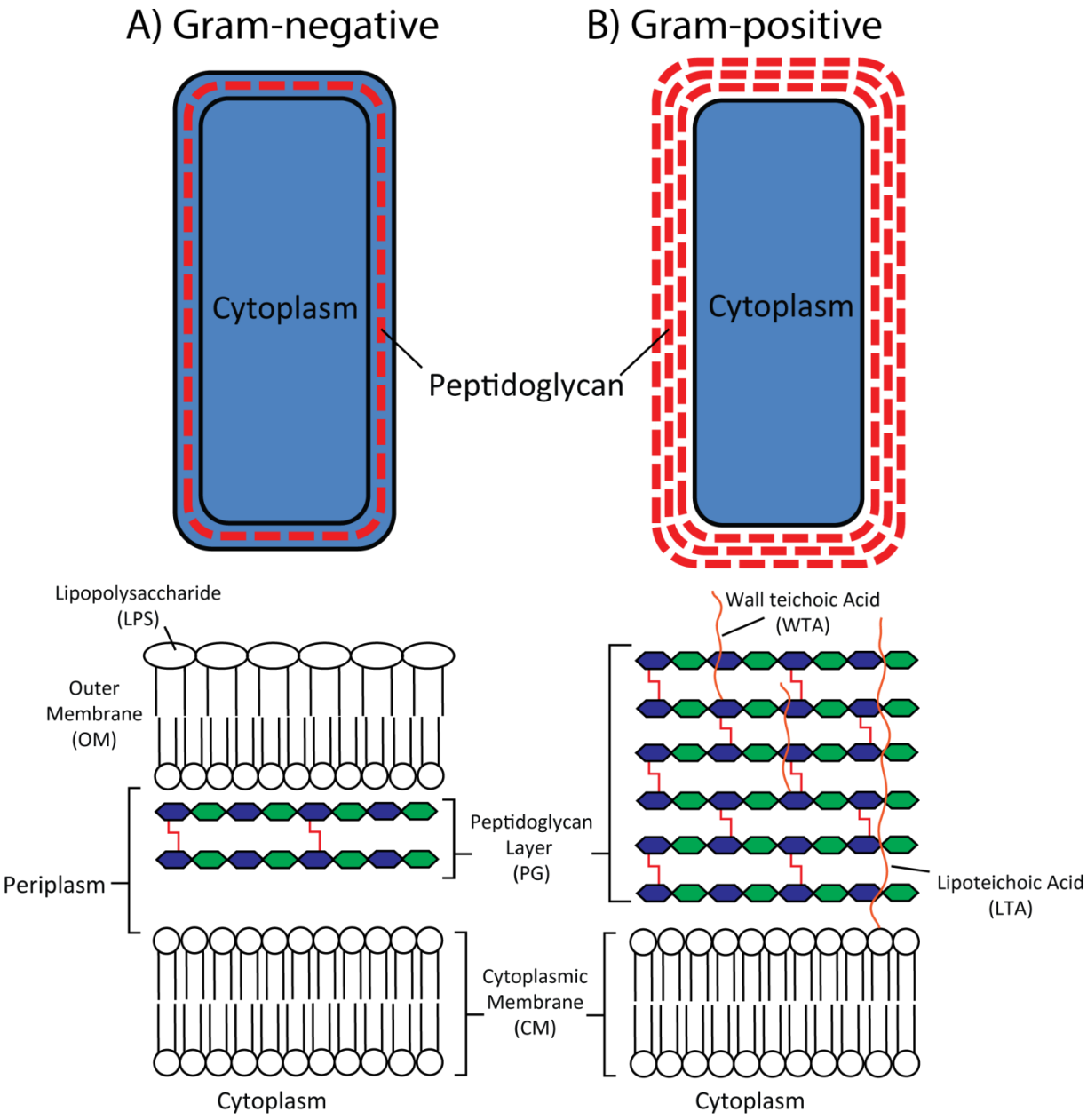

Figure 1.1 Structure of the Gram-negative (A) and Gram-positive (B) cell envelope. For the cartoon diagrams at the top, a black line represents a lipid membrane. Blue hexagons represent N-acetylmuramic acid, and green hexagons represent N-acetylglucosamine. Red lines represent peptide cross-links.

The peptidoglycan layer itself is made of saccharide chains cross-linked with peptides. [16] The saccharide chain is made of a repeating disaccharide unit consisting of N-acetylmuramic acid (blue hexagons in Fig. 1.1) and N-acetylglucosamine (green hexagons). These saccharide chains are cross-linked with peptides consisting of L-alanine, D-alanine, glycine, D-glutamic acid, and L-diaminopimelic acid for *B. subtilis* 168. [17] For Gram-negative species, this meshwork is between 1.5-15 nm [16], while for Gram-positive species like *B. subtilis*, the peptidoglycan layer can have a thickness of 15-30 nm. [16]

The main difference between Gram-negative and Gram-positive bacteria, in regards to their cell envelope, is the presence of an additional lipid membrane in Gram-negatives. This creates a cellular medium in between the two membranes, called the periplasm, for Gram-negative species. The outer membrane (OM) of Gram-negative species is asymmetric. The outer leaflet is composed of lipopolysaccharide (LPS), which is not found in Gram-positive bacteria. Gram-positive species have teichoic acids, which are negatively charged polymers attached to either the peptidoglycan wall (wall teichoic acid, WTA), or attached to a lipid molecule (lipoteichoic acid, LTA). For *B. subtilis* 168, this polymer is made of a poly(glycerol phosphate) chain. [18] The exact function of the teichoic acids is an active area of research, but they may play a role in cation homeostasis.

The lipid membrane compositions of Gram-negative and Gram-positive species also differ considerably. For *E. coli*, the cytoplasmic membrane consists of ~80% of the neutral lipid phosphatidylethanolamine (PE), 15% of anionic phosphatidylglycerol (PG), and 5% of anionic cardiolipin (CL). [19] For *B. subtilis* 168, the membrane composition is ~36% PG, 22% cationic lysyl-phosphatidylglycerol (LPG), 30% PE, and 12% CL. [20] The common factor between both membranes is anionic phospholipids, which are not found in as high of abundance in eukaryotic cell membranes. The cell envelopes of both Gram-negative and -positive species are highly negatively charged, which why cationic antimicrobial peptides have a preference for bacterial membranes instead of eukaryotic membranes. [12]

Antimicrobial Peptides (AMP's)

As of 2014, the Antimicrobial Peptide Database contains 2408 peptides, derived from animals, plants, fungi, and even bacteria. [21] The range of structures and sequences of these peptides is large and diverse. [22] While they can inhibit or kill bacteria *in vitro*, they also have immunomodulatory effects *in vivo*. [23] We will explore the current state of research on these molecules, and explain how our work will help illuminate new details on the mechanism of action of these peptides.

When considering AMP's, we must specify what class of molecules we are referring to. Lysozyme has antimicrobial properties, and is also a protein, but it is not part of the class of AMP's that we will discuss here. While lysozyme exerts some of its antimicrobial potency by cleaving the bond between N-acetylglucosamine and N-acetylmuramic acid in the peptidoglycan layer, our discussion of AMP's focuses on those that interact with bacterial membranes. This class of AMP's have a few general properties: they can form an amphipathic structure (the folded peptide exhibits two different "sides", one predominately hydrophilic, and the other hydrophobic [12], they are highly cationic, and they have the ability to permeabilize lipid membranes. Several models have been suggested as to how the peptides permeabilize membranes at the molecular level [13, 24], shown in Fig. 1.2. Barrel-stave pores (Fig. 1.2A) are characterized by the peptide oriented perpendicular to the plane of the bilayer, with the hydrophobic side facing the lipid tails, and the hydrophilic side facing the water channel. Toroidal pores (Fig. 1.2B) are similar to barrel-stave pores, except the lipids are curved such that the hydrophilic head groups face the inside of the channel. The carpet mechanism (Fig. 1.2C) is characterized by a general, "detergent like" solubilization of the membrane, with the formation of micelles. Considerable research has gone into studying the mechanism and structure of the disruption in model lipid bilayers, as well as studying their effects on bacteria.

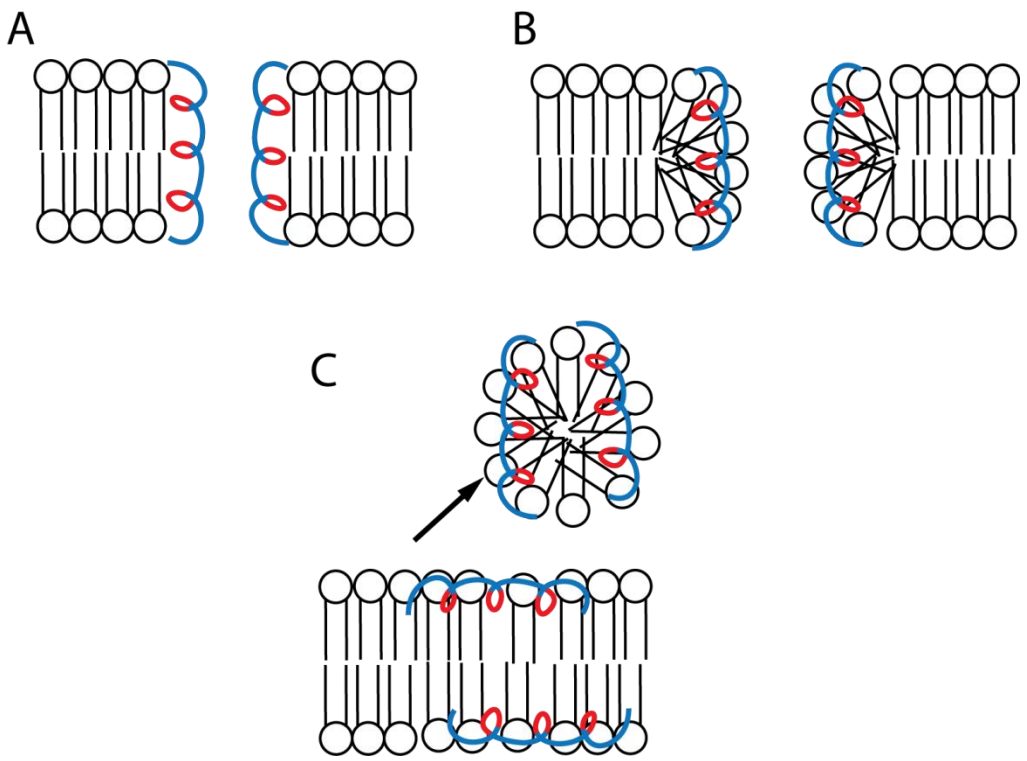

Figure 1.2 Proposed models of lipid bilayer disruption by α-helical AMP's, including A) barrel-stave pore, B) toroidal pore, and C) carpet mechanism with micellization. The blue color in the peptide represents hydrophilic residues, while red represents hydrophobic residues.

One of the methods used to assess antimicrobial activity on bacteria is the Minimum Inhibitory Concentration (MIC) assay. [25] In this assay, bacterial cells are inoculated into individual wells containing growth medium and varying amounts of the antimicrobial substance. The bacterial culture is then grown for a variable amount of time (6 to 24 hours), and cell growth is assessed via optical density. The lowest concentration of the antimicrobial substance that results in no visible cell growth is the MIC. While this method is useful for assessing the toxicity of a compound, it does not reveal much information as to how the compound is killing cells. We consider our experiments to be a more mechanistic version of the MIC.

Fluorescence Microscopy and Growth Conditions

The biophysical method we employ in our research is time-lapse fluorescence microscopy. With the advent of sensitive EMCCD cameras, powerful lasers, and fluorescent probes like green fluorescent protein (GFP) and DNA stains, fluorescence microscopy can be performed with remarkable sensitivity. Fluorophores are a less toxic way to image cells, compared to electron microscopy on fixed cells. The use of fluorescence microscopy, coupled with flow chambers that allow a constant replenishment of growth medium and oxygen, allow us to image cells with minimal perturbations, other than the desired antimicrobial stress. A picture of our experimental setup is given in Figure 1.3. Our microscope setup allows us to image cells prior to, and within ~1 min of, the introduction of an antimicrobial peptide into the flow chamber.

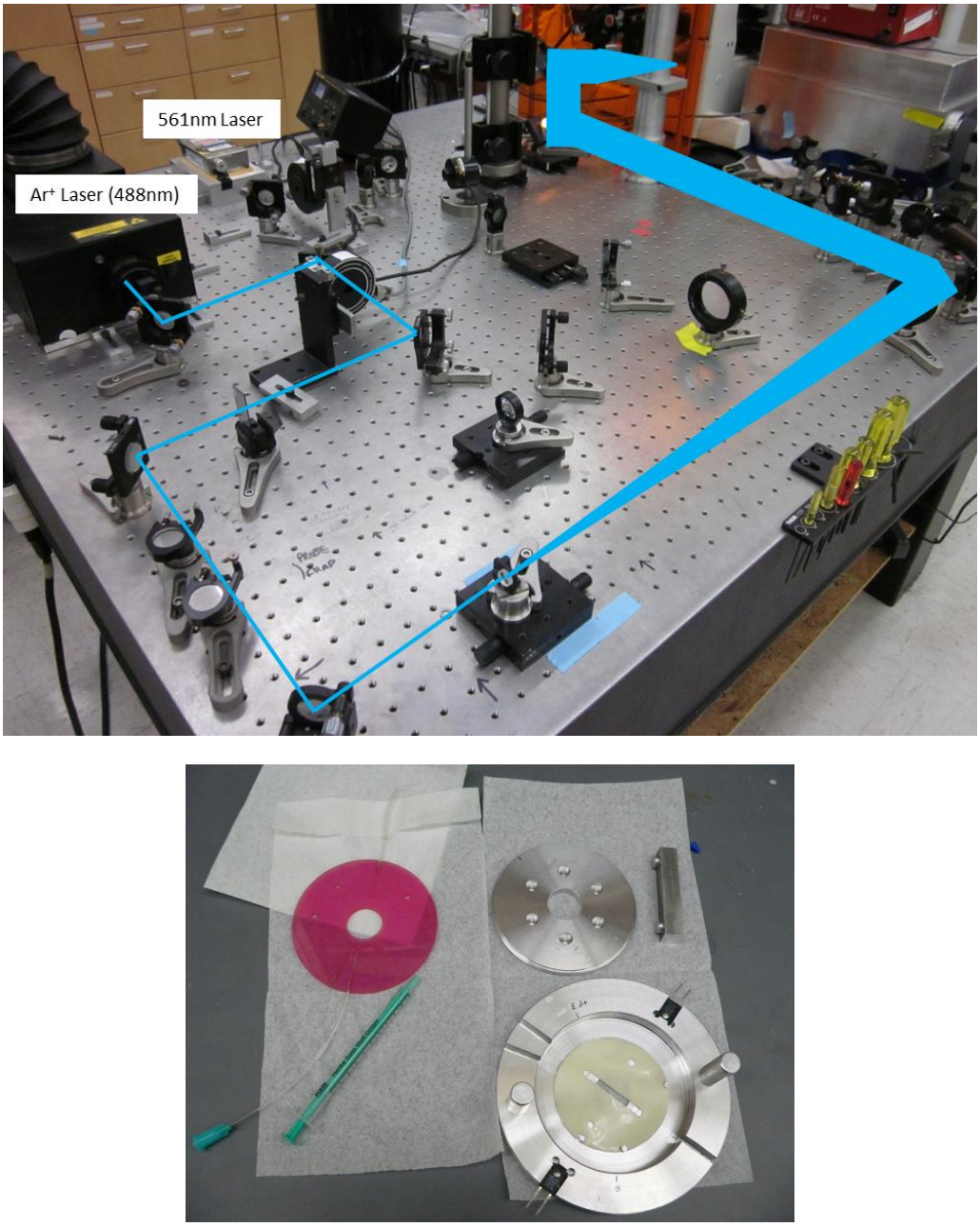

Figure 1.3 Top: fluorescence microscopy setup. The 488 nm laser path is shown by the blue lines. The 488 nm laser is used to image cytoplasmic GFP or the DNA stain Sytox Green. The 561 nm laser is used to image Sytox Orange. Bottom: flow chamber used for experiments. The white gasket shown at bottom right defines the height of the chamber. The pink plastic piece contains the tubing necessary for introduction of growth medium.

Traditional growth media for bacteria give fast doubling times, but are not amenable to fluorescence microscopy. They contain contaminants that cause background fluorescence, and their exact chemical composition is undefined. A chemically defined minimal medium (such as Spizizen's medium for *B. subtilis* [26]), will have little background fluorescence, but will give slow doubling times and reduce experimental throughput. Ideally, we would like a rich, chemically defined medium that has low background fluorescence, and provides doubling times similar to those of rich, undefined media (~20 min).

A growth medium meeting these properties was designed in the 1970's for *E. coli*, formulated by Neidhardt et al. [27] Our lab refers to this growth medium as EZRDM (EZ Rich Defined Medium). EZRDM contains carbon, nitrogen, sulfur, and phosphorus sources, necessary trace metals, amino acids, vitamins, and nucleotide bases. While this medium works well for *E. coli*, the concentrations of several components are not optimal for the growth of *B. subtilis*. As an example, EZRDM has the amino acid serine at a concentration of 5.26 mg/mL, while the optimum concentration for *B. subtilis* is 50 μg/mL or less. [28] Concentrations of amino acids above the recommended values can reduce the growth rate of *B. subtilis*.

To fix this issue, we modified the concentrations of several components in EZRDM to better suit the nutritional needs of *B. subtilis*, based on data given in Ref [28]. We call this modified growth medium *subtilis*-EZRDM, or *s*-EZRDM. The exact recipe, as well as the concentrations of the individual components, is given in Tables 1.1 to 1.3. A visual comparison between a chemically undefined growth medium (LB) and *s*-EZRDM is given in Fig. 1.4. The doubling time of *B. subtilis* in s-EZRDM at 37°C is ~20 min, the same as *B. subtilis* in LB at the same temperature.

Amount (mL)	Chemical or Supplement
5	10X MOPS Buffer mix
0.5	20% w/v Glucose
0.5	0.2 M K_2HPO_4
0.5	100X Trace Metals
1	4 M NaCl
10	5X EZ Supplement Beta
5	10X ACGU Beta

Table 1.1 Recipe for *s*-EZRDM. All solutions are made in ultrapure (18 MΩ) water. The above solutions are added to a 50 mL volumetric flask, and diluted to the mark with ultrapure water. *s*-EZRDM should be filter sterilized, not autoclaved. The recipe for the 100X Trace Metals solution is given in Table 1.2.

Chemical Compound	g/L (1000X solution)	Final Concentration of Trace Metal in 1X *s*-EZRDM (μM)
$CaCl_2{\cdot}2H2O$	6.00	51.3
$MnCl_2{\cdot}4H_2O$	1.00	5.1
$ZnCl_2$	1.70	12.5
$CuCl_2{\cdot}2H_2O$	0.43	2.53
$CoCl_2{\cdot}6H_2O$	0.60	2.55
$Na_2MoO_4{\cdot}2H_2O$	0.60	2.48
$FeSO_4{\cdot}7H_2O$	10.3	47.0

Table 1.2 Recipe for the stock solutions needed to make the 100X Trace Metals solution. Each metal salt is dissolved in ultrapure water by itself. The $FeSO_4{\cdot}7H_2O$ stock solution requires concentrated sulfuric acid to induce solubility (8 drops per 100 mL of solution made). The 100X Trace Metals solution can be made by adding 1 mL of each solution to a 10 mL volumetric flask, and diluting to the mark with ultrapure water. Note that the 10X MOPS buffer mix also contains small amounts of the above trace metals. The 100X Trace Metals solution is added to bring the final concentrations of these metals in 1X *s*-EZRDM (right column) close to the final concentrations that would be achieved if using the Trace Metals solution found in Ref [28].

Chemical Compound	Concentration (mM) in 1X *s*-EZRDM	Chemical Compound	Concentration (mM) in 1X *s*-EZRDM
NH_4Cl	9.5	2,3 dihydroxy Benzoic Acid	0.010
H_3BO_3	4.0×10^{-4}	Alanine	0.561
3-(N-morpholino) propanesulfonic acid (MOPS)	40	Arginine HCl	0.237
Tricine	4	Asparagine	0.378
Na_2SO_4	0.276	Aspartic Acid, K^+ salt	2.290
$MgCl_2 \cdot 6H_2O$	0.526	Cysteine HCl, H_2O	0.251
NaCl	80.0	Glutamic Acid, K^+ salt, H_2O	2.460
K_2HPO_4	2	Glutamine	0.342
Glucose	11.1	Glycine	0.666
Adenine	0.148	Histidine HCl, H_2O	0.239
Cytidine	0.206	Isoleucine	0.381
Guanine	0.132	Leucine	0.381
Uracil	0.357	Lysine HCl	0.342
Methionine	0.335	Phenylalanine	0.303
Proline	0.434	Serine	0.476
Threonine	0.420	Tryptophan	0.098
Tyrosine	0.110	Valine	0.427
Thiamin HCl	0.010	Calcium Pantothenate	0.010
Para-amino Benzoic Acid	0.010	Para-hydroxy Benzoic Acid	0.010

Table 1.3 Final concentrations of components in 1X *s*-EZRDM. Chemicals with a yellow background come from the MOPS buffer mix, chemicals in green are from solutions made by the user, chemicals in blue come from ACGU Beta, and chemicals in orange come from EZ supplement Beta.

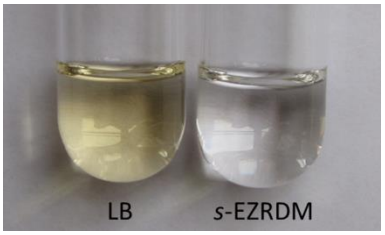

Figure 1.3. Visual comparison between *s*-EZRDM and a chemically undefined medium, LB.

References

1. **Control, C.F.D., *Achievements in Public Health, 1900-1999: Control of Infectious Diseases.* Morbidity and Mortality Weekly Report (MMWR), 1999. 48(29): p. 621-629.**

2. **Wainwright, M., *Miracle Cure: The Story of Penicillin and the Golden Age of Antibiotics*1990: Basil Blackwell.**

3. **Amyes, S.G.B., *Magic Bullets Lost Horizons: The Rise and Fall of Antibiotics*2001: Taylor & Francis.**

4. **Tipper, D.J. and J.L. Strominger, *Mechanism of action of penicillins: a proposal based on their structural similarity to acyl-D-alanyl-D-alanine.* Proceedings of the National Academy of Sciences of the United States of America, 1965. 54(4): p. 1133-41.**

5. **Tomasz, A., A. Albino, and E. Zanati, *Multiple antibiotic resistance in a bacterium with suppressed autolytic system.* Nature, 1970. 227(5254): p. 138-40.**

6. **Moreillon, P., et al., *Two bactericidal targets for penicillin in pneumococci: autolysis-dependent and autolysis-independent killing mechanisms.* Antimicrobial agents and chemotherapy, 1990. 34(1): p. 33-9.**

7. **Bayles, K.W., *The bactericidal action of penicillin: new clues to an unsolved mystery.* Trends in microbiology, 2000. 8(6): p. 274-8.**

8. **Novak, R., et al., *Signal transduction by a death signal peptide: uncovering the mechanism of bacterial killing by penicillin.* Molecular cell, 2000. 5(1): p. 49-57.**

9. **Kohanski, M.A., et al., *A common mechanism of cellular death induced by bactericidal antibiotics.* Cell, 2007. 130(5): p. 797-810.**

10. **Hong, H.A., et al., *Bacillus subtilis isolated from the human gastrointestinal tract.* Research in microbiology, 2009. 160(2): p. 134-43.**

11. **Tam, N.K., et al., *The intestinal life cycle of Bacillus subtilis and close relatives.* Journal of bacteriology, 2006. 188(7): p. 2692-700.**

12. **Zasloff, M., *Antimicrobial peptides of multicellular organisms.* Nature, 2002. 415(6870): p. 389-95.**

13. **Brogden, K.A., *Antimicrobial peptides: pore formers or metabolic inhibitors in bacteria?* Nat Rev Microbiol, 2005. 3(3): p. 238-50.**

14. **Whatmore, A.M. and R.H. Reed, *Determination of turgor pressure in Bacillus subtilis: a possible role for K+ in turgor regulation.* Journal of general microbiology, 1990. 136(12): p. 2521-6.**

15. **Cayley, D.S., H.J. Guttman, and M.T. Record, Jr., *Biophysical characterization of changes in amounts and activity of Escherichia coli cell and compartment water and turgor pressure in response to osmotic stress.* Biophysical journal, 2000. 78(4): p. 1748-64.**

16. **Vollmer, W., D. Blanot, and M.A. de Pedro, *Peptidoglycan structure and architecture.* FEMS microbiology reviews, 2008. 32(2): p. 149-67.**

17. **Atrih, A., et al., *Analysis of peptidoglycan structure from vegetative cells of Bacillus subtilis 168 and role of PBP 5 in peptidoglycan maturation.* Journal of bacteriology, 1999. 181(13): p. 3956-66.**

18. **Schirner, K., et al., *Distinct and essential morphogenic functions for wall- and lipo-teichoic acids in Bacillus subtilis.* The EMBO journal, 2009. 28(7): p. 830-42.**

19. **Morein, S., et al., *Wild-type Escherichia coli cells regulate the membrane lipid composition in a "window" between gel and non-lamellar structures.* The Journal of biological chemistry, 1996. 271(12): p. 6801-9.**

20. **den Kamp, J.A., I. Redai, and L.L. van Deenen, *Phospholipid composition of Bacillus subtilis.* Journal of bacteriology, 1969. 99(1): p. 298-303.**

21. **Database, A.P. [cited 2014 06/08/14]; Available from: http://aps.unmc.edu/AP/main.php.**

22. **Boman, H.G., *Peptide antibiotics and their role in innate immunity.* Annual review of immunology, 1995. 13: p. 61-92.**

23. **Bowdish, D.M., D.J. Davidson, and R.E. Hancock, *Immunomodulatory properties of defensins and cathelicidins.* Current topics in microbiology and immunology, 2006. 306: p. 27-66.**

24. **Shai, Y., *Mode of action of membrane active antimicrobial peptides.* Biopolymers, 2002. 66(4): p. 236-48.**

25. **Andrews, J.M., *Determination of minimum inhibitory concentrations.* J Antimicrob Chemother, 2001. 48 Suppl 1: p. 5-16.**

26. **Anagnostopoulos, C. and J. Spizizen, *Requirements for Transformation in Bacillus Subtilis.* Journal of bacteriology, 1961. 81(5): p. 741-6.**

27. **Neidhardt, F.C., P.L. Bloch, and D.F. Smith, *Culture medium for enterobacteria.* J Bacteriol, 1974. 119(3): p. 736-47.**

28. Cutting, S.M. and C.R. Harwood, eds. *Molecular Biological Methods for Bacillus*. 1990, John Wiley & Sons.

Chapter 2

Real-Time Effects of LL-37 on *Bacillus subtilis*

Introduction

Antimicrobial peptides (AMPs) are components of the innate immune system of many organisms, including insects, mammals, and amphibians [1, 2]. AMPs function as both antimicrobial agents and modulators of the immune system. While there is considerable diversity in the sequence and structure of these peptides, most have a net positive charge, a mixture of cationic and hydrophobic residues, and an amphipathic structure when bound to model lipid bilayers. The net positive charge allows the peptides to preferentially interact with the negatively charged surfaces of bacteria in favor of the more neutral surfaces of eukaryotic cells. However, the detailed mechanism(s) by which AMPs disrupt bacterial membranes and kill cells are not well understood [3, 4].

Standard bulk culture measurements of AMP activity include the minimum inhibitory concentration assay (MIC) and the minimum bactericidal concentration assay (MBC) [5]. The MIC is the concentration above which cell growth is not observed over a specified number of hours (usually 6 to 24 h) in the continuing presence of AMP. The (typically larger) MBC is the concentration at which cells removed from the AMP-containing medium do not produce new colonies on fresh agar plates lacking the AMP. It is often observed that *L*- and *D*- optical isomers of the same antimicrobial peptide have very similar MIC values. This strongly suggests that the growth-halting mechanism is primarily biophysical, rather than some specific mode of binding to a particular protein [6]. There are exceptions to this observation, as some AMPs have been shown to inhibit peptidoglycan synthesis [7]. Many of the proline rich AMP's have been shown to have a non-membrane permeabilizing mechanism of action, and do not exhibit similar MIC values for optical isomers of the peptide [6]. Real time RT-PCR performed on *B.*

subtilis exposed to the AMP's LL-37 and PG-1 have suggested that AMPs cause significant changes in gene expression by triggering stress-related signaling pathways [8].

Experiments that study AMP interactions with model lipid bilayer systems have provided important structural characterization by NMR, oriented circular dichroism, and x-ray and neutron scattering. Different mechanisms of membrane disruption have been proposed, including localized pore formation [9], global lipid segregation [10], and carpet- or detergent-like micellization [11]. For the human antimicrobial peptide LL-37 of interest here, there has been debate about its mechanism of membrane disruption. Some work supports a carpet model for membrane disruption [12, 13], while other work supports the pore mechanism [14, 15]. In a complementary method, molecular dynamics simulations using an atomistic model of melittin in a lipid bilayer strongly suggests that localized AMP-induced membrane disruptions have ill-defined structures only vaguely reminiscent of well-defined barrel-stave or toroidal pores [16]. Similar results were found for the shape of the pores formed by magainin [17]. The relevance of studies of model lipid bilayers to real bacterial membranes remains an open question.

We are developing single-cell, time-resolved fluorescence microscopy techniques that provide a new window on AMP interactions with live bacterial cells. A combination of imaging methods monitors cell length and membrane permeabilization events over time in each individual cell. Our initial study [18] of the attack of the α-helical AMP LL-37 and a rhodamine-labeled derivative (Rh-LL-37) on the Gram-negative *E. coli* showed that cell growth halted when Rh-LL-37 translocated across the outer membrane to gain access to the periplasm. This occurred long before permeabilization of the cytoplasmic membrane. On translocation Rh-LL-37 binds to immobile elements within the periplasm. We suggested that the growth-halting mechanism was interference with peptidoglycan synthesis.

Here we present a detailed study of the effects of LL-37 on the model Gram-positive bacterium *Bacillus subtilis*. Our data suggests two different mechanisms of growth inhibition depending on the bulk LL-37 concentration. At 2 μM LL-37 (twice the 6-hr MIC), the cell growth rate decreases without

permeabilization of the membrane to the small dye Sytox Green. At 4 μM LL-37, cells abruptly shrink and Sytox Green gains entry to the cytoplasm, indicating loss of turgor pressure and presumably loss of the transmembrane potential. In a novel "recovery assay", we remove the LL-37 after a fixed interaction time and monitor cells for recovery of normal growth over several hours. The growth-slowing symptom at 2 μM LL-37 is reversible for at least some cells, while the abrupt permeabilization symptom at 4 μM is not.

Materials and Methods

Chemicals

Solid LL-37 was purchased from Anaspec (95% pure, Catalog no. 61302, Fremont, CA) and used without further purification. A 1 mM stock solution of LL-37 was made from 1 mg LL-37 and sterile, ultrapure (18 MΩ) water. This solution was separated into 50 μL aliquots, and stored at -20 °C until needed. LL-37 composed of all D-amino acids (D-LL-37) at 92% purity was made by the University of Wisconsin-Madison Biotech center and stored the same way. A 5 mM Sytox Green solution in DMSO was purchased from Molecular Probes (Catalog no. S7020, Grand Island, NY). The sodium salt of nigericin was purchased from Sigma Aldrich (Catalog no. N7143, St. Louis, MO) and dissolved in ethanol. Supplements used for the media (5X EZ supplement Beta, M3104; 10X ACGU Beta, M3103; 10X MOPS mix, M2137) were purchased from Teknova (Hollister, CA).

Strains and Growth Conditions

B. subtilis 168 from the Bacillus Genetic Stock Center (BGSC, code 1A1) was used as the wild type strain. Plasmid pAD43-25 [19], also from BGSC, produces GFPmut3 under the control of a constitutive promoter. Our *B. subtilis* strain was made competent and then transformed with pAD43-25 based on the two-step method found in Molecular Biological Methods for *Bacillus* [20]. The strain with pAD43-25 was grown and imaged with 5 μg/mL chloroamphenicol to select for the plasmid. All strains were grown in *subtilis*-EZRDM at 37 °C and 200 rpm (0.9 g) in a New Brunswick Excella E24 Incubator-

Shaker. Cultures were grown in *s*-EZRDM overnight, inoculated from a frozen glycerol culture. The following day, dilutions of at least 1/200 were made into pre-warmed *s*-EZRDM. Cells were grown to an OD of 0.04–0.06 (600 nm, 1 mm path length) as measured on a Nanodrop 2000 from Thermo Scientific, and then harvested for microscopy or MIC measurements.

Minimum Inhibitory Concentration (MIC) Assay

MICs were measured only on wild type *B. subtilis*. A serial dilution of either LL-37 or D-LL-37 was performed in one row of a polystyrene 96-well plate in *s*-EZRDM, beginning at 32 μM and with twofold dilution at each step. The final volume in each well in the row was 50 μL after serial dilution. A liquid cell culture was grown in the same conditions as described in "Strains and Growth Conditions," to a final OD of 0.04–0.06. This culture was diluted in *s*-EZRDM to an OD of 0.005. 50 μL of the diluted culture was added to each well of the LL-37 serial dilution, so that the maximum concentration tested was 16 μM. The final OD in each well was 0.0025, and the final volume in each well was 100 μL. A second row contained 50 μL of *s*-EZRDM plus 50 μL of inoculum (positive growth control), while a third row contained 100 μL of *s*-EZRDM in each well (negative growth control and blank for OD measurements). The plate was incubated at 37 °C while shaking at 200 rpm (0.9 g) in an Excella 24 Incubator/Shaker from New Brunswick Scientific for up to 12 h. The "6-hr MIC" is reported as the lowest concentration for which no cell growth could be detected after 6 h, as determined by measurements of OD at 595 nm using a Wallac EnVision 2100 Multilabel Reader from Perkin–Elmer. The MIC experiments were performed three times, and were reproducible to within a dilution factor of two. D-LL-37 and LL-37 had the same 6-h MIC of 1 μM.

Microscopy Experiments

All microscopy experiments were carried out at 37 °C. The home built, temperature-controlled flow chamber, with an internal volume of ~60 μL, was described previously [18]. The only modification was coverslip preparation. We initially tried poly-L-lysine coated slides to immobilize cells for observation, but found that *B. subtilis* had difficulty growing on this surface. Instead, coverslips were

sonicated for 30 min in acetone, rinsed with ultrapure water, and dried with nitrogen gas. Cells harvested from the mid-log phase liquid culture were diluted 1/6 in pre-warmed *s*-EZRDM, then injected into the flow chamber. The cells were rinsed with at least 0.8 mL of fresh medium to remove unadhered cells. The 0.5 mL antimicrobial solution, also made with *s*-EZRDM, contained both LL-37 and 0.5–1 nM Sytox Green, unless otherwise stated. This solution was vortexed for at least 10 s to break up possible aggregates of LL-37. Time-lapse imaging began when a region with a suitable density of plated cells was found. LL-37/Sytox Green was injected 7.5 min after the beginning of the movie; the injection itself required ~20 s. The growth medium was subsequently static after injection.

Time-lapse, widefield imaging of a field of single cells monitored entry of Sytox Green into the cytoplasm by the onset of its green fluorescence, as well as cell length and width vs time by phase contrast imaging. In some experiments, Sytox Green was omitted and cytoplasmic GFP was imaged in the green channel. The Nikon Eclipse TE300 microscope was equipped with a Nikon Phase Contrast Type DLL Objective, NA = 1.3 and an Andor iXon 897 EMCCD camera. All fluorescence images were taken using 488 nm excitation light from an Ar^+ laser at an intensity of 6.6 W/cm^2 at the focal plane where the cells were imaged. A 500 nm long-pass filter (HQ500LP, Chroma Technology) was used in the microscope dichroic cube. Emission filters (also from Chroma) were HQ510/20 M for Sytox Green, and ET525/50 M for cytoplasmic GFP. Phase contrast images were collected with the same emission filter used to image the corresponding fluorescence channel.

Most time lapse movies were obtained as follows. A 50-ms fluorescence image was taken, followed 6 s later by a 50-ms phase contrast image. This 12-s imaging cycle was repeated 300 times to obtain a 1 h movie. A few of the growth control movies used an 18 s cycle time. Faster movies focusing on the staining dynamics of Sytox Green (but still including alternate phase contrast images) were obtained with a 2-s cycle time. The fastest movies with a 0.5-s cycle time imaged only the green fluorescence.

The environment inside the chamber is temperature controlled and contains a rich medium, but the experiments presented here were performed under static conditions. We are unable to flow LL-37 continuously due to the large volume of injection solution needed and the cost of the peptide. The *B. subtilis* cells in the chamber are presumably growing anaerobically during most of the observation period, since oxygen is not continuously replenished. *B. subtilis* can grow anaerobically through fermentation if both glucose and all 20 amino acids are provided [21], as in our growth medium. The doubling time of the cells in the static flow chamber is approximately 60 min, three times longer than the 20-min doubling time in aerated liquid culture. When *B. subtilis* cells are grown in the chamber with a continuous flow of aerated medium, the doubling time matches the liquid culture doubling time, suggesting that interaction with the glass surface does not impede growth.

Data Analysis

Movies from time-lapse imaging were analyzed using ImageJ [22], and the program MicrobeTracker [23] using algorithm 4 with modifications to the following parameters: areaMin = 300, thresFactorM = 1.2, thresFactorF = 1.2, splitThreshold = 0.5, joindist = 8, joinangle = 1.2. MicrobeTracker calculates cell length and volume for each cell at all frames. Cell width *w* was calculated as the average of the width measurements obtained from the MicrobeTracker meshes over the central 60% of the cell length *L*. This ensured the endcaps were excluded from the width measurements. Width measurements were also performed using ImageJ on fluorescence images of GFP in the strain of *B. subtilis* producing cytoplasmic GFP. The width estimates from the two methods were consistent with one another. The values of cell length, width, and volume calculated from MicrobeTracker were compared to a spherocylinder model to confirm that the program was returning reasonable data (Appendix 2A). Relative cell length vs time was calculated as L_{total}/L_0, where L_{total} is the sum of the tip-to-tip lengths of the original cell plus any daughter cells it created and L_0 is the length of the cell at the beginning of the movie. Relative changes in cellular dimensions as calculated by MicrobeTracker are quite reliable, while the absolute values depend somewhat on parameters chosen within the program.

Results

Effects of LL-37 on Growth of Individual Cells

We have studied the effects of LL-37 on the growth of single *B. subtilis* cells in the concentration range 0 to 4 μM (up to four times the 6-h MIC of 1 μM). A total of 62 cells were analyzed (0 μM LL-37, $N = 9$; 1 μM, $N = 15$; 2 μM, $N = 21$; 4 μM, $N = 17$). LL-37 and *D*-LL-37 yielded similar results. Figure 2.1 shows the typical effects of LL-37 on the growth of individual cells. A representative example from a "growth control" experiment (medium with no LL-37 injected) is shown in Fig. 2.1 A-C. This particular cell forms an obvious septum at $t \sim 30$ min and eventually divides. Sytox Green staining does not occur, as shown by the absence of Sytox Green fluorescence (Fig. 2.1B). Cell length and cell volume, as measured by MicrobeTracker, are presented in Fig. 2.1C. The red lines represent exponential fits to the data, using the exponential growth function $Y(t) = Y_0 \exp[(t - t_0)/\tau]$, where Y represents either cell length (L) or volume (V). Here t_0 is the time at which observation begins and Y_0 is the length or volume of the cell at t_0. The only fitting parameter is the base-e time constant τ. The time constant τ is related to the more typically reported doubling time t_d as: $t_d = \tau \ln 2 = 0.693\ \tau$. For this particular cell, a good fit is obtained with the value t = 77 min (t_d = 54 min) for cell length, and t = 68 min (t_d = 47 min) for cell volume. Volume is not proportional to length due to endcap effects.

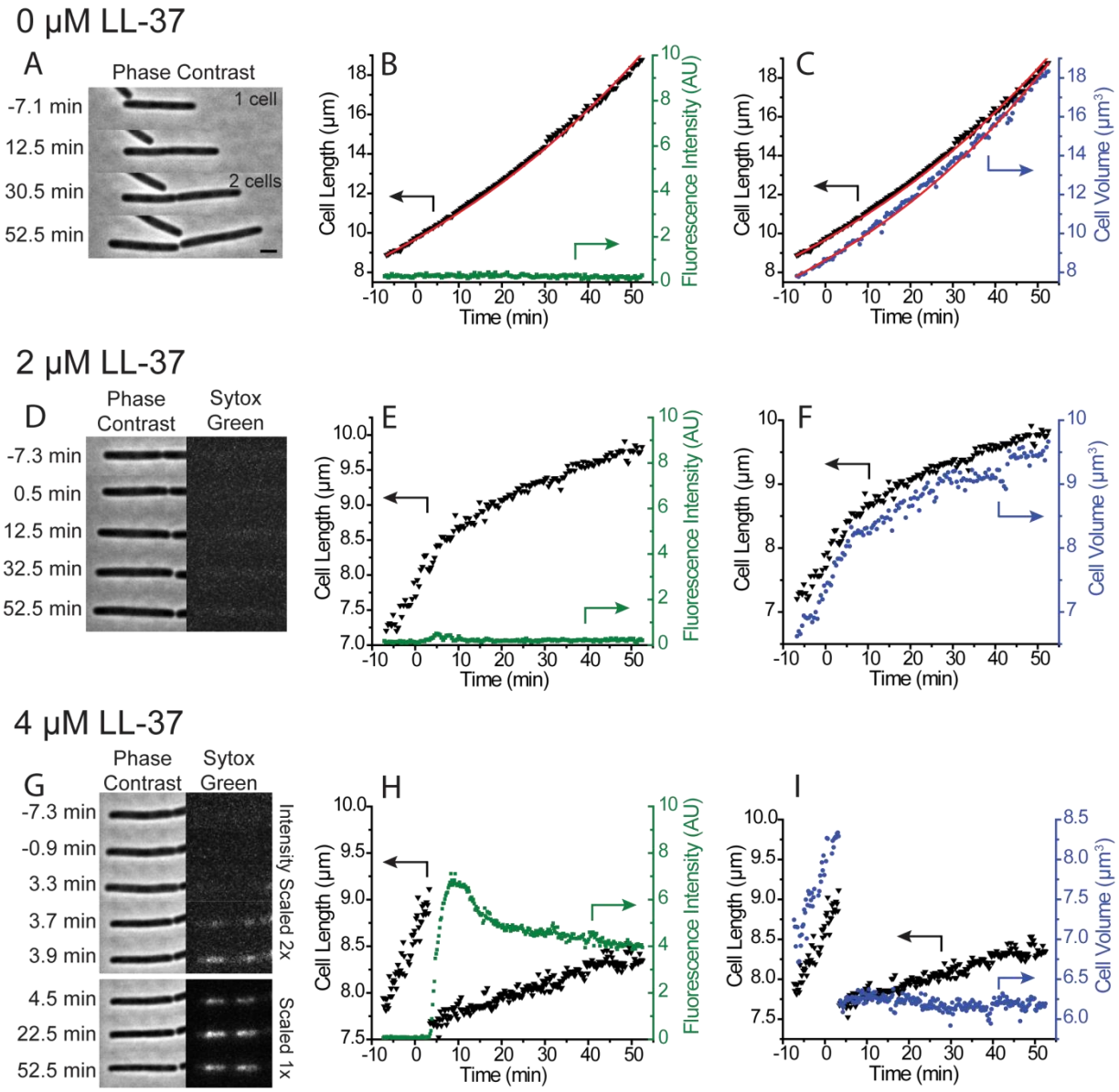

Figure 2.1: Imaging and analysis of one typical cell for LL-37 concentrations of 0 µM (panels A-C), 2 µM (D-F), and 4 µM LL-37 (G-I). Column at left shows phase contrast and green fluorescence images vs time. Middle column shows cell length (inverted triangles, left axis) and integrated Sytox Green fluorescence intensity (green circles, right axis) vs time. Column at right shows cell length (inverted triangles, left axis) and cell volume (blue squares, right axis) vs time. The red lines in B and C are exponential fits to the length data. Scale bar is 2 µm.

An example of the effects of 2 μM LL-37 (twice the 6-h MIC) on *B. subtilis* growth in the flow chamber is shown in Fig. 2.1D-F. Prior to injection and for a lag time of ~5 min after injection, the length increases vs time with a slope reminiscent of unperturbed growth. At t ~ 5 min after injection the *curvature* turns negative rather abruptly while the length continues to increase, *i.e.*, the growth *rate* decreases. The cell continues to lengthen, albeit more and more slowly, over the entire 50 min of observation after injection. The cell evidently maintains much of its biopolymer content throughout, as evidenced by the absence of apparent changes in phase contrast between the cytoplasm and the surrounding medium. As shown in the green fluorescence images (Fig. 2.1D) and the integrated Sytox Green intensity plot vs time (Fig. 2.1E), the cell nucleoid is not stained with Sytox Green, a cell-impermeant nucleic acid stain with a higher affinity for DNA than RNA [24]. Cells should exhibit nucleoid staining only if the barrier function of the plasma membrane has been compromised to Sytox Green. Evidently, cell growth rate is attenuated by 2 μM LL-37, but the barrier function of the membrane is maintained, at least to Sytox Green. The estimated radius of Sytox Green is ~1 nm [25], assuming a spherical molecule. Cell volume and cell length vs time (Fig. 2.1F) exhibit similar curves, indicating that real growth (increasing volume) is occurring.

The observations are very different at 4 μM LL-37 (four times the 6-h MIC), as shown in Fig. 2.1G-I. At t = 3.5 min after injection of LL-37, the cell length shrinks abruptly by 16%, while the width shrinks by 7% (Fig. 2.1G and H). The change in cell width is calculated for the frames immediately before and after shrinkage. This abrupt shrinkage typically occurs in less than one imaging cycle (<12 s). Within 10-20 s of the cell shrinkage event, the Sytox Green fluorescence signal begins a sharp rise, direct evidence of membrane permeabilization (Fig 2.1H). The cytoplasm still maintains its overall biopolymer density as judged by phase contrast images, which indicates that most cytoplasmic components remain within the cell wall. We interpret the abrupt shrinkage as arising from membrane permeabilization and loss of turgor pressure, as discussed in detail below.

A surprising behavior at 4 μM LL-37 is the gradual increase in cell length immediately *after* the shrinkage event, as shown in Fig. 2.1I. While the cell never achieves its pre-shrink length over the 50-min observation time, the increase in length could mean that cell growth has been reestablished, albeit at a slower rate than before introduction of LL-37. However, the volume measurements (Fig. 2.1I) show no appreciable change in cell volume after cell shrinkage, indicating no real cell growth. While cell length is increasing, the cell width is decreasing in a way that preserves volume. Values of cell length, width, and volume before and after shrinkage can be found in Appendix 2B, and confirm our hypothesis about cell volume preservation.

In order to test whether or not the membrane *remains* permeable after the shrinkage event, we performed experiments in which 4 μM LL-37 in growth medium without Sytox Green was injected at t = 0, and Sytox Green in growth medium was injected at varying delay times after all of the cells in the field of view had shrunk. Without Sytox Green, cell length again slowly recovered after abrupt shrinkage, indicating that Sytox Green was not causing the slow length recovery. When 1 nM Sytox Green was injected either ~5 min or ~40 min after the last cell in the field of view had shrunk (t = 10 min or 45 min, respectively), visible staining of the nucleoid again occurred within ~20 s of Sytox Green injection. These experiments demonstrate that the loss of membrane integrity is irreversible on the 50-min time scale, *i.e.*, the membrane does not re-establish its barrier function to molecules the size of Sytox Green.

We also measured several length vs time curves at 8 μM LL-37 without Sytox Green (Appendix 2C). Abrupt shrinkage events occur earlier at this higher concentration (within ~1 min for 8 μM LL-37, compared to ~3 min for 4 μM LL-37). In contrast to the typical behavior at 4 μM LL-37, there was little or no recovery of length after shrinkage. We discuss possible interpretations of the length and volume behavior below.

Comparisons Between Cells

Thus far we have presented data on single cells, to show the level of information we can acquire from these experiments. In Fig. 2.2 we compare length vs time plots for a number of cells observed at

LL-37 concentrations of 0, 1, 2, and 4 μM. Because cells have different lengths prior to injection, we plot the relative cell length $L(t)/L_0$, where L_0 is the length at the beginning of the movie (t_0, prior to injection). If all cells grew exponentially at the same rate, then all of the $L(t)/L_0$ plots would superimpose.

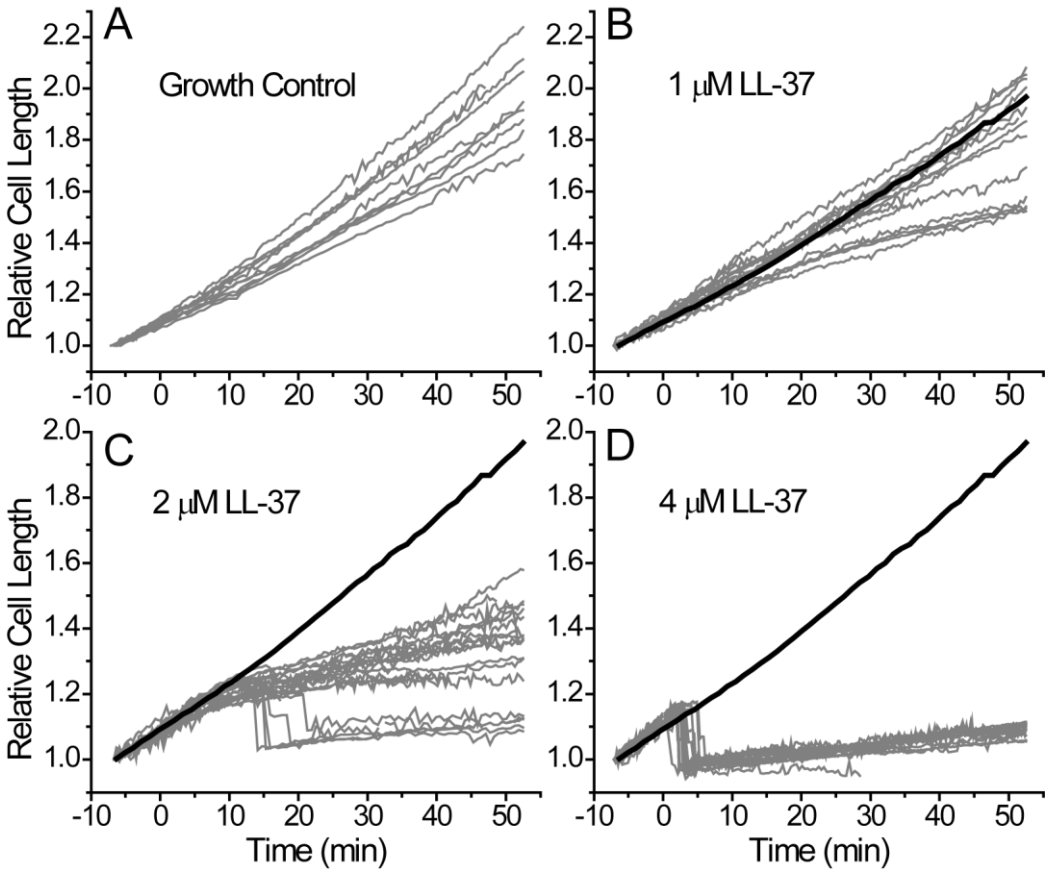

Figure 2.2 Plots of relative cell length $L(t)/L_0$ vs time over 60 min for 62 *B. subtilis* cells at (A) 0 μM, (B) 1 μM, (C) 2 μM, and (D) 4 μM. LL-37 was injected at $t = 0$. L_0 is the cell length at $t = -7$ min, the beginning of the observation period. The mean of the best-fit base-*e* growth time constants for the growth control curves in panel A is t = 85 ± 10 min (± 1 standard deviation). For reference, the mean of the growth control curves in panel A is shown in panels B, C, and D as the heavy black line.

As estimated from length, the growth control curves (0 μM LL-37, Fig. 2.2A) have a mean value of the base-*e* growth time constant of $\langle\tau\rangle = 85 \pm 10$ min (± one standard deviation), corresponding to a

mean doubling time of $<t_d>$ = 59 ± 6 min. The modest dispersion may be due to natural variations among cells or to mild heterogeneities within the sample cell. As a reference, the mean of all 9 growth control curves is plotted as a heavy black line in the plots of $L(t)/L_0$ for non-zero LL-37 concentrations.

At 1 μM LL-37 (equal to the 6-h MIC value, Fig. 2.2B), some cells continue to grow normally throughout the 50-min observation period while approximately one-third of the cells show mild growth rate attenuation. The signature of growth rate attenuation is the change in curvature of $L(t)/L_0$ from positive to negative. Sytox Green never stains the nucleoid at 1 μM LL-37. At 2 μM LL-37 (Fig. 2.2C), ~70% of cells exhibit growth rate attenuation without Sytox Green staining. The growth rate attenuation is more severe than at 1 μM LL-37. About 30% of the cells exhibit abrupt shrinkage and subsequent Sytox Green staining. At 4 μM LL-37 (Fig. 2.2D), all of the cells exhibit shrinkage and Sytox Green staining. The mean lag time between LL-37 injection and shrinkage is 3.5 ± 1.2 min. After shrinkage, most cells exhibit a modest recovery of cell length over 50 min. At 8 mM LL-37 (Appendix 2C), all cells shrink abruptly with a mean time to shrinkage of 0.8 ± 0.2 min. There is little or no evidence of gradual recovery of length after shrinkage at 8 μM LL-37.

In Fig. 2.2, the experiment was repeated at least 3 times for each of the four different concentrations. All the data are combined. The variability in Fig. 2B, C, and D is primarily due to variation between individual experimental runs, rather than cellular heterogeneity within a single experiment. Appendix 2D shows this in greater detail. The cause of the experimental variability may be our inability to prepare uniformly active LL-37 samples, variable loss of peptide to the surfaces of the sample chamber, or inherent day-to-day variability in growing of *B. subtilis* cultures.

Localized Sytox Green Staining Events

As visualized by Sytox Green fluorescence at long times, most cells under these growth conditions exhibit two major nucleoid lobes (Fig. 2.1G). For longer cells, each lobe shows evidence of partial segregation into two sub-lobes. The fast movies of Fig. 2.3 demonstrate that at 4 μM LL-37, the initial entry of Sytox Green into the cytoplasm is localized. Using 2 s/frame time resolution, ~50% of the

cells show initial staining in a single punctum, followed by a gradual spreading of intensity to the rest of the nucleoid. The other half of the cells exhibit two or more puncta, and only one or two cells in the group of 28 observed cells showed apparent "global" staining (staining without initial spatial localization.) In the example of Fig. 2.3A, staining begins at the endcap of the cell and spreads to completely stain all nucleoid lobes in 1.6 min. This is an example of initial staining at one punctum. In the example of Fig. 2.3B, staining begins at both endcaps almost simultaneously, and then moves towards the middle of the cell to completely stain all nucleoid lobes.

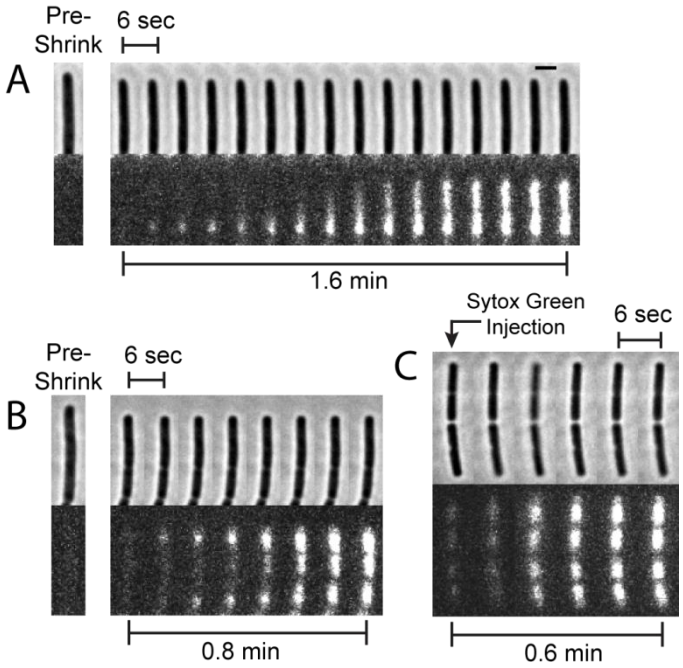

Figure 2.3 Sytox Green images vs time after abrupt shrinkage events using 4 mM LL-37. Images were acquired every 2 s, but only every third frame is shown in the sequence of images (6-s spacing). (A) An example of localized staining that begins at a single pole, and subsequently spreads to the rest of the nucleoid. The scale bar of 2 μm also applies to the images in B and C. (B) Example of localized staining beginning at both poles. (C) Example of a more global staining pattern when Sytox Green is added 45 min after introduction of LL-37, long after the shrinkage event. Staining begins simultaneously at all four nucleoid lobes and is not localized.

As an additional experiment, we injected Sytox Green ~45 min after introduction of LL-37, well after cell shrinkage (Fig. 2.3C). At these long time delays, Sytox Green staining was rapid, but was more global than punctal. The more global staining pattern might be due to global disruption of membrane function to molecules the size of Sytox Green. It may also be due to one local, highly permeable patch that admits Sytox Green so rapidly that we do not catch the localized staining in time.

The initially punctal staining pattern fits a model in which Sytox Green enters the cytoplasm through a small membrane patch, binds locally to DNA, gradually saturates the local binding sites, and then spreads outward in space to find additional binding sites until the entire nucleoid lobe is saturated. In such a model, the time scale on which the staining coats the entire nucleoid lobe depends on many factors, including the Sytox Green bulk concentration, the permeability of the small patch, and the binding/diffusion kinetics of Sytox Green within the cytoplasm. These factors combine to determine the observed ~1 min time scale for complete staining.

In the earliest image showing clear Sytox Green staining, the puncta are typically round but not diffraction limited. Even at 2 s/frame, the initial full width at half-maximum (FWHM) intensity is typically about 500 nm. Because the FWHM of the point-spread function is ~250 nm, we estimate an upper limit on the breadth of the source of the fluorescence as ~400 nm. Because the Sytox Green will spread out in space after entry into the cytoplasm, the small size of the initial staining patch sets an upper bound on the size of the initially permeabilized membrane patch. Localized staining implies localized membrane permeabilization, but diffraction-limited fluorescence microscopy cannot determine whether the initially permeabilized membrane patch is a pore or a disordered local disruption of the membrane. We can only say that the small size of the initial Sytox Green/DNA patch is consistent with pore formation.

Gradual Permeabilization to Larger Species at Long Times by LL-37 at 4 μM

We carried out several experiments using 4 μM LL-37 on cells expressing GFP in the cytoplasm. To avoid interference in the green channel, no Sytox Green was added. A fluorescence intensity vs time

trace for a single cell is shown in Fig. 2.4. In all cells observed (N = 9) with 12-s cycle time between frames, the GFP fluorescence intensity first decreased by ~20–30% in one camera frame, coincident in time with the instant of cell shrinkage, and then abruptly leveled off. As argued below, we believe the abrupt decrease in intensity at the time of shrinkage is a photophysical effect, i.e., that it is not due to loss of GFP from the cytoplasm. At much longer times, t ~ 15-50 min after injection, the remaining GFP signal was lost. This loss occurs gradually over 5 to 10 min; the trace shows rounded edges at the beginning and end. We attribute this second loss of GFP fluorescence to *delayed* permeabilization of the membrane to GFP. It should be noted that for molecules the size of GFP, it is possible that the peptidoglycan layer may act as a permeability barrier along with the membrane.

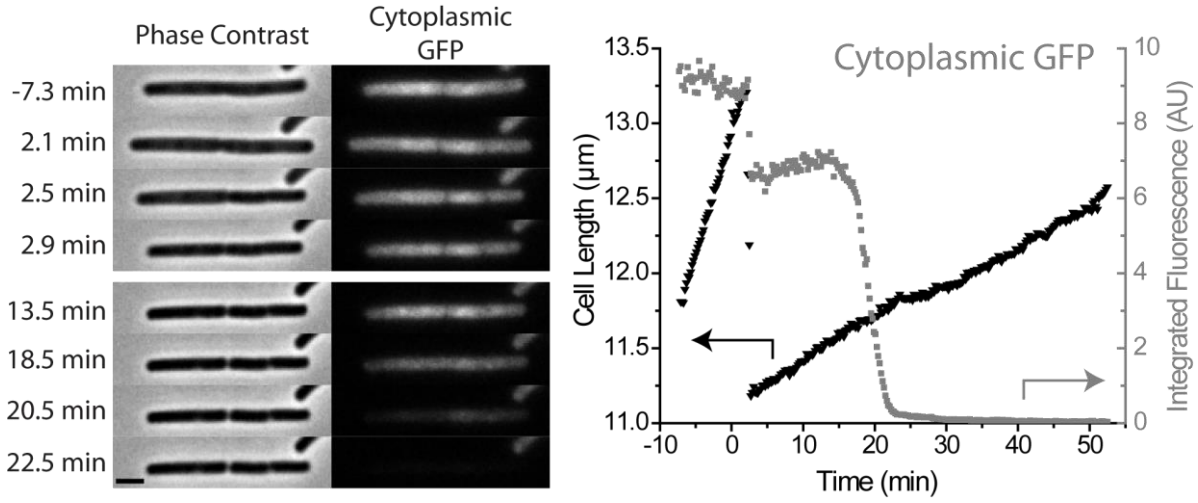

Figure 2.4. Typical effects of 4 μM LL-37 cells expressing cytoplasmic GFP. Black inverted triangles are cell length (left axis) and Cytoplasmic GFP fluorescence is shown by gray squares (right axis). Two shrinkage events occur in rapid sequence (see frames at 2.5 and 2.9 min after injection of LL-37). This indicates the presence of a complete septum between two joined cells. GFP intensity decreases abruptly at the moment of cell shrinkage due to photophysical effects. A second decrease in GFP intensity occurs after a 15 min delay, over a period of ~10 min. This is due to delayed permeabilization of the membrane to GFP. Scale bar is 2 μm.

The 20–30% loss of GFP intensity at the time of shrinkage occurred in a single camera frame even when the frame time was as short as 0.5 s (Appendix 2E). If this were due to loss of GFP, it would require much of the GFP to find the localized permeabilization patch in < 0.5 s. While we have found no measurements of the diffusion constant of GFP inside the cytoplasm of *B. subtilis* in the literature, the diffusion constant of GFP in *E. coli* has been found to range from ~4-14 $\mu m^2/s$ [26, 27]. Even at 14 $\mu m^2/s$, it would not be possible for the GFP to diffuse through the localized permeabilization patch in less than half a second. The argument is presented in detail in Appendix 2F. Instead, we believe that the abrupt decrease in cytoplasmic pH during the shrinkage event causes a decrease in GFP quantum yield. Our medium is buffered at pH 7.4, which leads to an internal pH of ~7.8-8.1 [28, 29]. When the membrane is permeabilized, the pH in the cytoplasm will abruptly decrease by ~0.5 pH units to the pH of the buffered medium. The particular GFP used here, GFPmut3, is known to be sensitive to pH with decreasing fluorescence intensity as pH decreases, the same direction as our observations [30].

As an additional test, we carried out experiments injecting the drug nigericin, which eliminates the ΔpH across the membrane by exchanging K^+ for H^+ across the membrane [31, 32]. As shown in Appendix 2G, 5 μM nigericin leads to an approximately 30% decrease in GFP signal for the cell shown; all cells analyzed showed a 25-35% loss of GFP signal. For nigericin treatment, there is never complete loss of GFP at longer times after shrinkage (up to 1 hr). Separate experiments confirmed that after nigericin treatment, Sytox Green did not enter the cytoplasm up to 52.5 min after injection.

In one experiment, cells not expressing GFP were incubated in 4 μM LL-37 without Sytox Green and observed for longer periods of 2-3 h. Cells abruptly shrank at t ~ 2-4 min as usual. For the two cells shown in Fig. 2.5, beginning at t ~ 80 min, we observed yet another behavior in which the shrunken cells lost phase contrast over a period of ~70 min. The time at which loss of phase contrast begins and the length of time over which it is lost is highly variable across cells and individual experimental runs. Similar results were obtained with cells producing cytoplasmic GFP.

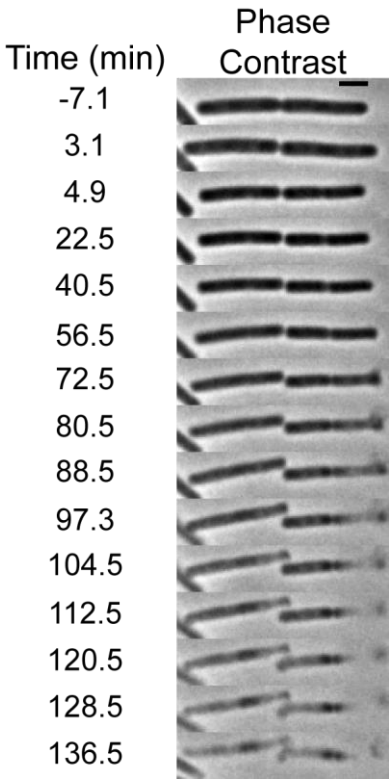

Figure 2.5. Long-time phase contrast images of two cells treated with 4 μM LL-37. Loss of phase contrast begins at about 80 min and continues over at least one hour. Scale bar is 2 μm.

To summarize, 4 μM of LL-37 *gradually* causes permeabilization of the membrane to larger and larger species over a period of hours. Simultaneous with the shrinkage event, Sytox Green permeates the membrane locally; the pH presumably equilibrates across the membrane at the same time. The membrane is permeabilized to proteins the size of GFP only much later, ~10-50 min after LL-37 addition. Localized Sytox Green staining is not observed when Sytox Green is injected ~45 min after LL-37 introduction (presumably when cytoplasmic GFP has already been lost). Still later, at t ~ 90 min, even ribosomes permeate the membrane. It is important to note that at some point during the gradual increase in permeabilization, the peptidoglycan layer will also act as a permeability barrier. In order for large, 20-nm diameter species [33] like ribosomes to escape from the peptidoglycan layer, the natural mesh size of the

layer must expand [34]. We suspect that the driving force for this breakdown in the peptidoglycan layer is autolysis, [35, 36] as further explored in the discussion section.

Recovery Experiments

For all data reported thus far, *B. subtilis* cells are incubated in LL-37 throughout the entire observation period, as would occur in an MIC assay. In the following "recovery" experiments, cells in the flow chamber are incubated at a given LL-37 concentration for a period of time, and then rinsed with fresh, aerated growth medium. Sytox Green is not present. Observation by phase contrast continues for 2-3 h, depending on the time scale of symptoms. This is analogous to a single-cell minimum bactericidal concentration (MBC) assay. The goal is to determine the extent to which cells whose growth has been altered by LL-37 can recover and grow normally after restoration of aerated *s*-EZRDM growth medium.

In Fig. 2.6A, we show a cell incubated in 2 μM LL-37 beginning at $t = 0$ and then rinsed thoroughly at $t = 33$ min and again at $t = 58$ min. The rinses cause defocusing of the phase contrast image and small jogs in the $L(t)$ curve. As described previously, LL-37 changes the curvature of $L(t)$ (attenuates the growth rate) but does not entirely halt growth. Within ~20 min of rinsing with fresh growth medium, $L(t)$ again turns upward for the cell shown in Fig 2.6A. As judged by the base-*e* time constant $\tau = 113$ min, the cell has reestablished growth, albeit at a slower growth rate than if LL-37 had never been present. There is heterogeneity across cells in the recovery behavior at 2 μM LL-37. Some cells resume normal growth, as in Fig. 2.6A. Some cells abruptly shrink at longer time scales even though external LL-37 has been removed. Still other cells never resume growth during the observation period of 2-3 hr. Evidently an entire culture whose growth rate was attenuated by exposure to 2 μM LL-37 for ~30 min would readily recover after restoration of normal growth medium.

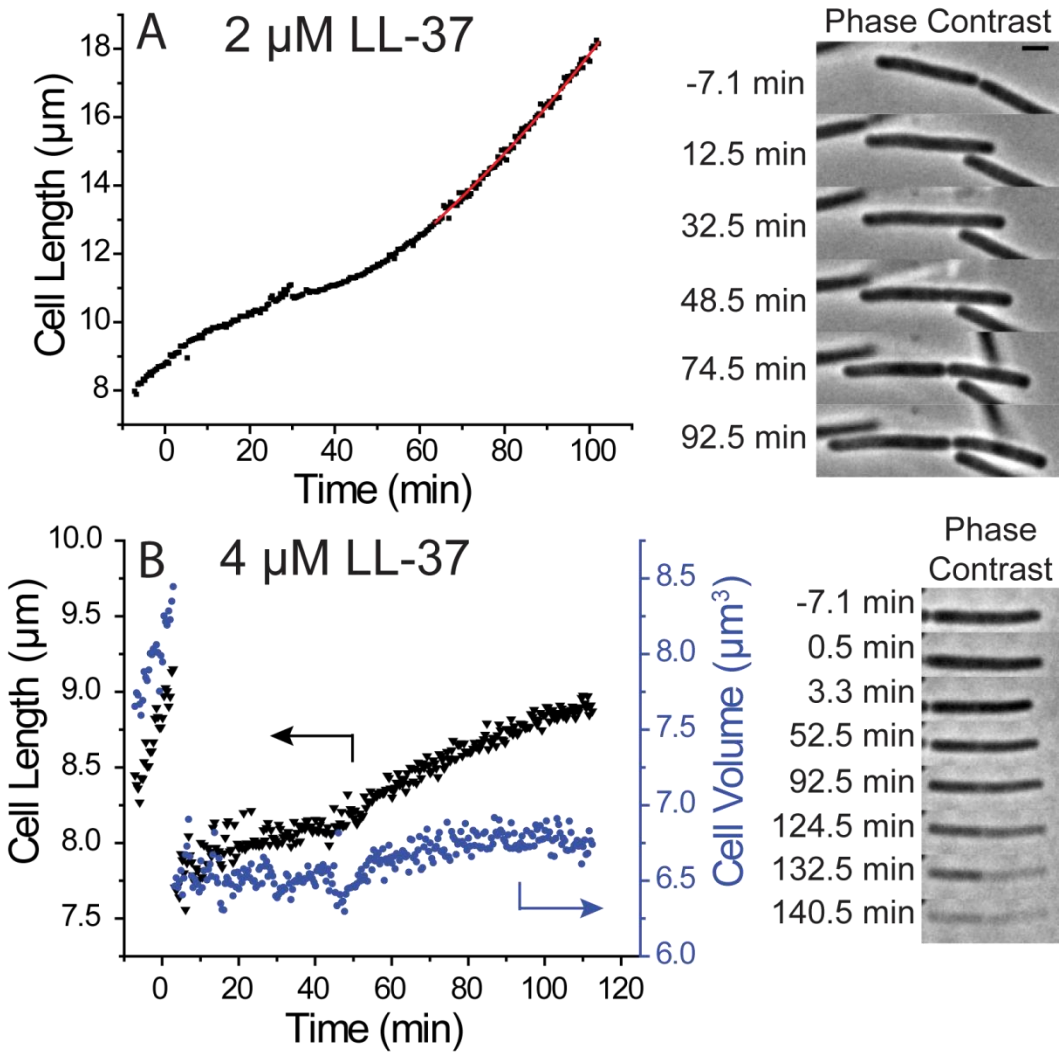

Figure 2.6. Recovery experiments at LL-37 concentrations of 2 μM (panel A) and 4 μM (panel B). *Left*: plots of cell length and volume vs time. *Right*: Phase contrast images vs time. For 2 μM LL-37, cells were rinsed first at 32.5 min and again at 57.5 min after injection. Growth resumes shortly after the initial rinse. For 4 μM LL-37, cells were rinsed first at 5.5 min and again at 12.5 min after injection. There is no clear evidence of growth, and at long times the cytoplasm loses phase contrast. Scale bar is 2 μm.

In contrast, Fig. 2.6B shows the recovery behavior of a cell initially incubated in 4 μM LL-37. In this experiment, all the observed cells suffered abrupt shrinkage events within 4 min of exposure to LL-37. The cells were rinsed with fresh, aerated growth medium at t = 6 min and again at t = 13 min. As

occurred without rinsing (Fig. 2.5), the typical rinsed cell (Fig. 2.6B) gradually lengthens after the shrinkage event, but never regains its pre-shrink length. The volume curve, although noisy, shows no clear evidence of real growth. Following the rinses, and beginning at about 60 min, this particular cell gradually loses phase contrast, suggesting substantial loss of biopolymer content. Of the 12 cells studied by the recovery method at 4 μM LL-37, all but one lost phase contrast before reaching the pre-shrink maximum length. This is essentially the same behavior observed without rinsing. None of the observed cells had resumed normal growth by the end of the observation period of 2-3 hr. Evidently the damage inflicted on the cell by exposure to 4 μM for only 6 min is permanent and irreversible, in contrast to that imposed by 2 μM for 30 min.

Discussion

Gradual Permeabilization to Larger Species at Long Times by LL-37 at 4 μM

The single-cell, real time assay reveals new layers of detail in the modes of attack of antimicrobial peptides on live bacterial cells. In earlier work [18], we studied the attack of LL-37 on the Gram-negative species *E. coli*. Rhodamine-labeled LL-37 (Rh-LL-37) at 8 μM (4 times the 12-h MIC of 2 μM) uniformly coats the cell outer membrane in less than 1 min. Cells that were already septating at t = 0 were subsequently attacked earlier than non-septating cells. After a lag time of about 10 min, Rh-LL-37 translocates across the outer membrane to enter the periplasm primarily at the septal region, which is evidently much more susceptible to translocation than mature outer membrane regions. Growth halts immediately thereafter, just before periplasmic GFP leaves the cell and long before permeabilization of the cytoplasmic membrane to Sytox Green. Below a threshold bulk Rh-LL-37 concentration of 4 μM (twice the MIC), the outer membrane was coated but growth did not halt. We speculated that the growth-halting mechanism involved interference with cell wall synthesis within the periplasm, perhaps due to binding of the highly cationic LL-37 to anionic components of the nascent peptidoglycan layer. Non-

septating cells appeared to continue to grow until septum formation, at which time LL-37 penetrated the outer membrane and growth halted.

Here we extend the work to the Gram-positive species *B. subtilis*, which has only one membrane. We find no evidence for preferential attack on septating vs non-septating cells, although we are insensitive to cell cycle due to phase contrast microscopy's limitations in visualizing septa in *B. subtilis*. For both Rh-LL-37 at 8 μM on *E. coli* and unlabeled LL-37 at 4 μM on *B. subtilis* (four times the MIC in both cases), we observe a several-minute time lag between injection of LL-37 and the halting of growth. In *E. coli*, the lag was dominated by slow translocation across the outer membrane to reach the periplasm. Bulk and surface-bound Rh-LL-37 rapidly establish an equilibrium [37]. At Rh-LL-37 bulk concentrations near the MIC, the surface concentration builds up quickly, but translocation and growth halting does not occur during a 60-min observation time. At 8 μM, the higher surface concentration led to translocation in septating cells, but only after a 10-min time lag. This is consistent with a cooperative model of translocation. It suggests that even when a critical surface concentration of Rh-LL-37 is present, multiple peptide molecules must come together and insert into the membrane, enabling facile translocation. Slow nucleation of this insertion step may explain the long time lag before translocation.

In the *B. subtilis* study we have avoided use of Rh-LL-37 because we did not observe the same set of symptoms as those induced by unlabeled LL-37. Rh-LL-37 did not cause the abrupt shrinkage step, even at concentrations as high as 24 μM. The abrupt, local membrane permeabilization step for *B. subtilis* at 4 μM of unlabeled LL-37 again exhibits characteristics consistent with a cooperative event [38] having a nucleation step as a bottleneck. Below a threshold bulk concentration, the membrane permeabilization step does not occur. At 4 μM and above, abrupt permeabilization always occurs, but only after a substantial time lag. The time lag might be due to slow adsorption of LL-37 into the peptidoglycan layer; without labels, we cannot discern the time scale of equilibration between bulk and surface LL-37. It may also be limited by slow diffusion of the highly positively charged LL-37 through the thick, negatively charged layer of mature peptidoglycan. Slow dissociation of helical bundles of LL-37 in the

peptidoglycan layer may also contribute; these bundles are stable in salty solution and may also be stable in the hydrophilic environment of the peptidoglycan layer.

Growth Rate Suppression at Low LL-37 Concentrations

At 2 μM of LL-37 on *B. subtilis* (twice the MIC), the concentration is evidently too low to induce permeabilization of the membrane. An alternative mechanism is observed (Fig. 2.1D-F). The growth *rate*, as measured by the slope of plots of cell length vs time, begins to decrease about 5 min after injection of LL-37. Cells grow more and more slowly over at least 50 min, and Sytox Green never enters the cytoplasm. One plausible cause of this behavior is direct interference with cell wall synthesis, analogous to the growth-halting mechanism proposed for *E. coli*. LL-37 presumably displaces the dipositive cations Mg^{2+} and Ca^{2+} within the peptidoglycan layer. A second possibility is transduction of a stress signal through the membrane [8], triggering a change in the transcription profile, and a decrease in the cell wall production rate. A third possibility involves a *gradual* decrease in the proton motive force across the bacterial membrane. This would lead to gradually decreasing intracellular levels of ATP, and a gradual decrease in growth rate. We tried to observe changes in internal pH at 2 μM LL-37 using the strain of *B. subtilis* expressing cytoplasmic GFP. Unfortunately, our assay is ineffective at measuring gradual changes in GFP intensity (and thus, internal pH), due to the competing effect of photobleaching. The cause of the gradual slowing of growth remains an open question.

Abrupt Shrinkage at High LL-37 Concentration

At 4 μM and 8 μM of LL-37, a lag time of a several minutes after injection is followed by abrupt shrinkage of all observed cells. LL-37 permeabilizes the membrane, which enables leakage of small molecules and ions from the cytoplasm to the surrounding medium. Much of the turgor pressure is lost. Sytox Green at 0.5-1 nM bulk concentration enters the cytoplasm and begins to stain the nucleoid less than 20 s after the shrinkage event. It takes about 5 minutes for the Sytox Green staining to reach its asymptotic value. Presumably a membrane permeable to Sytox Green is also permeable to protons, indicating that the cell membrane potential is abruptly lost as well. The phase contrast of the cytoplasm

relative to the surrounding medium shows no obvious change immediately after shrinkage, indicating that much of the biopolymer content remains within the cytoplasm.

Cell length shrinks by about 15% on average, while the width shrinks by about 6%, implying an overall volume decrease of 25%. The turgor pressure is assumed to drop uniformly across the peptidoglycan. Thus, the change in aspect ratio on loss of turgor suggests that the normal turgor pressure stretches the peptidoglycan layer more easily along the long axis than circumferentially.

At 4 μM LL-37 the abrupt shrinkage event is followed by a gradual recovery of cell length. This recovery does not occur at 8 μM LL-37. In the *E. coli* study, we often observed a similar shrinkage and partial recovery of cell length [37]. At least in the case of *B. subtilis*, the gradual length recovery is not due to real cell growth. The cell never regains its pre-shrink length over 50 min of observation. Importantly, cell volume does not increase during this slow increase in length (Fig. 2.1I). In addition, the membrane potential evidently remains zero after the abrupt permeabilization event, preventing ATP synthesis and also disrupting many crucial metabolic pathways. The experiments using delayed addition of Sytox Green after shrinkage of the cells confirm that the membrane barrier function is not restored during the period of slow length recovery. The delayed loss of cytoplasmic GFP indicates that cell wall damage gradually becomes more severe over tens of minutes. We do not understand the restoring force driving the slow length recovery. It could be due to gradual remodeling of the peptidoglycan layer by autolysins, whose activity continues even after the membrane potential is abolished.

Pore Formation?

The observed *localized* permeabilization of the membrane revealed by the initially punctal Sytox Green staining at 4 μM LL-37 is consistent with the hypothesis of pore formation. Accordingly, recent structural studies on model lipid bilayers indicate that LL-37 indeed forms pores [14]. However, our assay provides no detailed information about the structure of the localized membrane disruption in *B. subtilis*. We only know that it is small, at most about 400 nm in breadth, because the earliest images of DNA staining are round with full width at half-maximum intensity of ~500 nm. Different studies suggested

that LL-37 permeates model membranes by a "carpet" or "detergent-like" mechanism [12, 13]. The observed localized permeabilization events argue against this mechanism in real bacterial membranes.

The delayed loss of cytoplasmic GFP at $t \sim 30$ min (Fig. 2.4) and the even later loss of most cytoplasmic content at $t \sim 1.5$ h (Figs. 2.5 and 2.6B) indicates that LL-37 treatment slowly causes permeabilization of the membrane to larger and larger biomolecules, including ribosomes, over a period of several hours. This occurs both when the cells remain in contact with LL-37 and when the bulk LL-37 is rinsed away. The underlying mechanism of this slow membrane disruption is not clear. After the initial permeabilization event, the size limit on which cytoplasmic species are lost may be determined by the porosity of the peptidoglycan layer rather than the membrane itself. One possibility is that autolysins continue to degrade the peptidoglycan layer long after the onset of permeabilization and the halting of growth.

Recovery Assay

Here we introduced a rudimentary "single-cell minimal bactericidal concentration" (MBC) assay by injecting LL-37, allowing it to act over a variable period of time, rinsing the plated cells to remove bulk LL-37, and then observing whether or not cells recover and resume normal growth. Although 2 μM exceeds the 6-h MIC, the slowing of growth on a 30-min time scale at this concentration is a "recoverable" symptom for many cells. When fresh growth medium is restored, some cells return to normal growth over a period of ~30 min. We suspect that fresh medium is able to remove much of the LL-37 from the peptidoglycan layer, i.e., that binding to the cell wall is reversible. Because the symptoms observed in our 1-h observation period are reversible, the data do not reveal the mechanism by which 2 μM LL-37 halts growth over 6 h in the MIC assay.

The recovery experiments at 4 μM rinsed away bulk LL-37 just minutes after the shrinkage events. No cells were observed to recover and grow normally on a time scale of 2-3 hr. It seems clear that the abrupt permeabilization event is sufficient to kill cells. The reason that permeabilization is not a recoverable symptom is less clear. Possibilities include irreversible loss of critical cytoplasmic

components, irreparable damage to the cell wall by the action of autolysins, disruption of the membrane potential, or a combination of all of these effects.

Finally, we comment on the relationship between our 1-h, single-cell antimicrobial action assay and the time-honored minimum inhibitory concentration assay (MIC). The MIC is measured as the minimum antimicrobial concentration that inhibits growth over an extended time period, typically chosen as 6-12 h. For LL-37 on *B. subtilis* in *s*-EZRDM growth medium at 37ºC, our measured 6-h MIC is 1 μM, accurate within a factor of two. On the time scale convenient for these microscopy experiments, about 1 h, we observe only minor effects of 1 μM LL-37 on cell growth (Fig. 2.3). Our studies focused on the concentration range 2-8 μM, well above the 6-h MIC, because these concentrations yield measureable effects on a 1-h time scale. The effects observed on the 1-h time scale are very different at 1 μM, 2 μM, and 4-8 μM. This suggests that for concentrations above the MIC, the dominant microscopic mechanism of anti-bacterial action may vary substantially with increasing antimicrobial concentration. However, we cannot be certain that the microscope sample chamber maintains the initial bulk LL-37 concentration over long periods. It remains possible that the growth rate suppression observed at 1-2 μM is the real behavior at constant bulk concentrations just below the MIC and that the abrupt shrinkage observed at 4-8 μM is the real behavior at constant bulk concentrations just above the MIC.

Appendix 2A: Spherocylinder Model and Volume Measurements

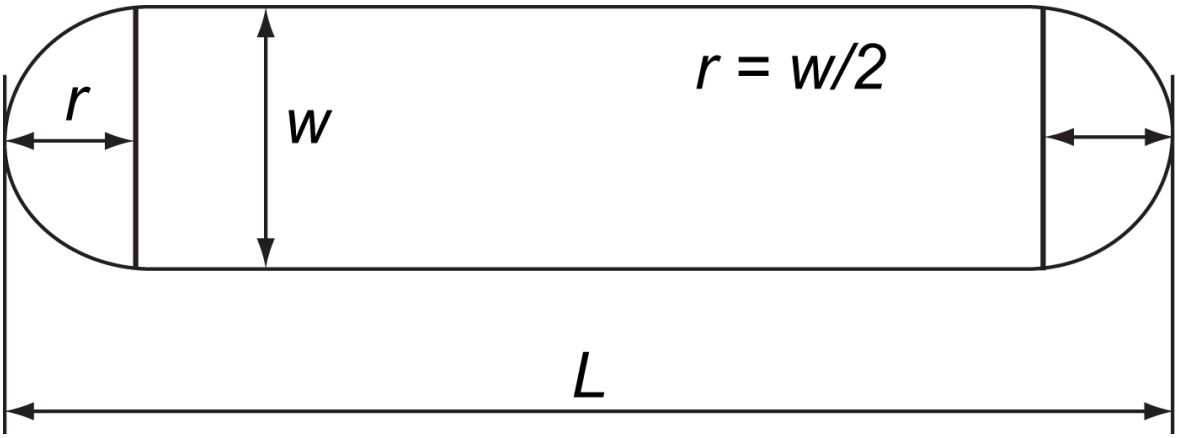

Figure 2A.1 Spherocylinder Model for Rod-Shaped Cells

A spherocylinder is a cylinder with 2 hemispherical endcaps. The volume of a spherocylinder is the sum of the volumes of a cylinder plus a sphere. The radius *r* of the sphere is half the width *w* of the cylinder. In terms of cell length *L* and cell width *w*, the parameters obtained from MicrobeTracker, the volume equals:

$$V = (\pi/4)w^2(L - w) + (\pi/6)w^3 \qquad \text{Eq. (2A.1)}$$

MicrobeTracker calculates cell volume, but not using Eq. 2A.1. Instead, MicrobeTracker divides the cell into small "slices", whose axes are perpendicular to the centerline of the cell. Each slice has a fraction of the total cell area, and has a fraction of the total cell volume, assuming symmetry of cell width around the centerline. The volumes of the cell slices are summed to get the total cell volume. A visual representation of this can be found on the MicrobeTracker website [39]. The cell volumes MicrobeTracker calculates agree with the volumes calculated using Eq. (2A.1) and the values of *w* and *L* obtained from MicrobeTracker to within 3% in all cases, as shown in Table 2A.1.

TABLE 2A.1 Volume Measurements of *B. subtilis* Cells

Cell #	Cell Length (μm)	Cell Width (μm)	Cell Volume (μm^3) From MicrobeTracker	Cell Volume (μm^3) From Eq. 2A.1
1	9.11	1.11	8.29	8.56
2	15.06	1.10	13.77	13.90
3	13.69	1.17	13.92	14.30
4	12.23	1.11	11.49	11.46
5	13.53	1.11	12.56	12.81
6	9.04	1.07	7.64	7.74
7	12.11	1.13	11.55	11.74
8	10.99	1.09	9.73	9.84
9	8.52	1.10	7.54	7.76

Appendix 2B: Volume Preservation after Cell Shrinkage

Cell #	Cell Dimensions (Pre-Shrink)				Cell Dimensions (Post-Shrink)				Cell Dimensions (~50 min After Shrinkage)			
	L	W	V (MT)	V (2A.1)	L	W	V (MT)	V (2A.1)	L	W	V (MT)	V (2A.1)
1	9.11	1.12	8.29	8.56	7.67	1.04	6.18	6.25	8.35	0.99	6.19	6.21
2	15.06	1.10	13.77	13.90	12.93	1.02	10.31	10.36	14.17	0.99	10.63	10.72
3	13.70	1.17	13.92	14.30	11.60	1.09	10.41	10.54	13.04	1.02	10.20	10.34
4	12.23	1.11	11.49	11.46	10.42	1.06	8.65	8.84	11.36	0.98	8.41	8.33
5	13.53	1.11	12.56	12.81	11.26	1.05	9.24	9.45	12.69	0.97	9.09	9.12
6	9.04	1.07	7.64	7.74	7.87	1.02	6.07	6.12	8.93	0.94	5.98	5.98
7	12.11	1.13	11.55	11.74	10.38	1.07	9.00	8.95	11.78	1.01	9.27	9.21
8	10.98	1.09	9.73	9.84	9.40	1.02	7.36	7.40	10.30	0.99	7.64	7.70
9	8.52	1.10	7.54	7.76	7.24	1.04	5.73	5.84	7.79	1.00	5.75	5.82

TABLE 2B.1 Volume Preservation at Long Times After Cell Shrinkage

Table 2.B1 lists the cell dimensions (length, width, and volume) of 9 cells before, after, and ~50 min after cell shrinkage. V(MT) is the volume estimate from MicrobeTracker, and V(2A.1) is the volume calculated from Eq. 2.A1. The two measurements of volume give the same conclusions on cell dimension. From Pre-Shrink to Post-Shrink, cell Length, Width, and Volume decrease by 15, 6, and 25%, respectively. From Post-Shrinkage to ~50 min after Shrinkage, the average cell width decreases by 6%, while average cell length increases by 11%. The average change in volume from Post-Shrink to ~50 min after Shrinkage is <1%, confirming that cell volume is constant even though cell width and length are changing post-shrinkage.

Appendix 2C: Cell Length vs. Time at 4 and 8 µM LL-37

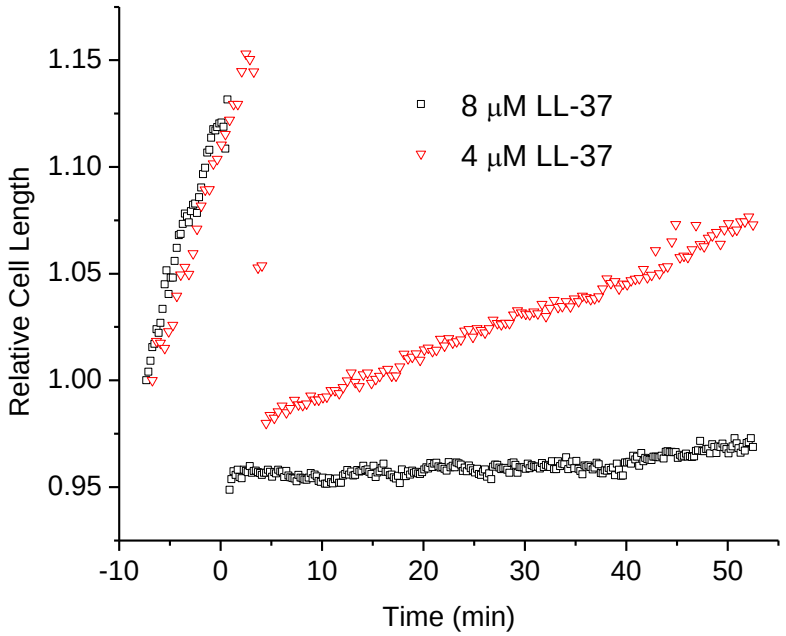

Figure 2C.1. Comparison of relative cell length vs time for two cells. One cell was exposed to 4 µM LL-37 (red triangles) and the other exposed to 8 µM (black squares) LL-37. The post-shrinkage increase in cell length is nearly zero when the LL-37 concentration is doubled.

Appendix 2D: Experimental Heterogeneity at 1 and 2 µM LL-37

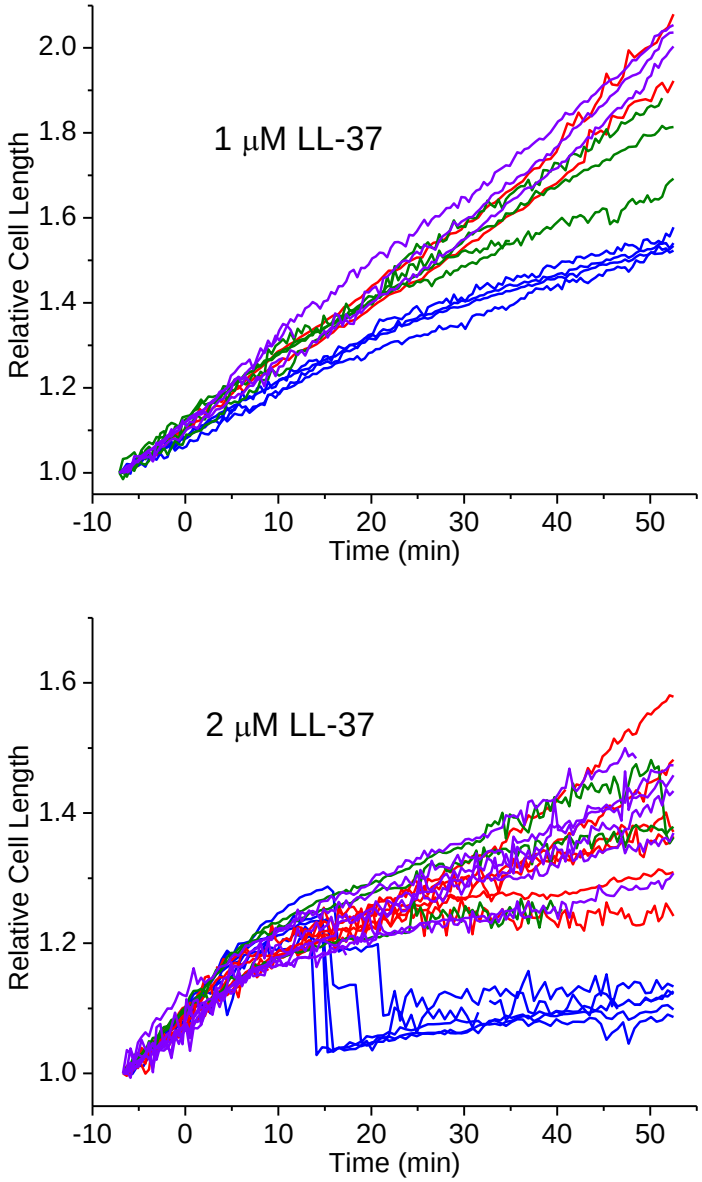

Figure 2D.1 Heterogeneity between experimental runs of 1 µM LL-37 (Top) and 2 uM LL-37 (Bottom). Cells belonging to a single experimental run are shown in the same color. The data set is the same as that used in Fig. 2.2. At 2 µM LL-37, the examples of cell shrinkage are all from the same experimental run, suggesting a higher effective LL-37 concentration in that run.

Appendix 2E: Fast Movies of GFP-producing *B. subtilis*

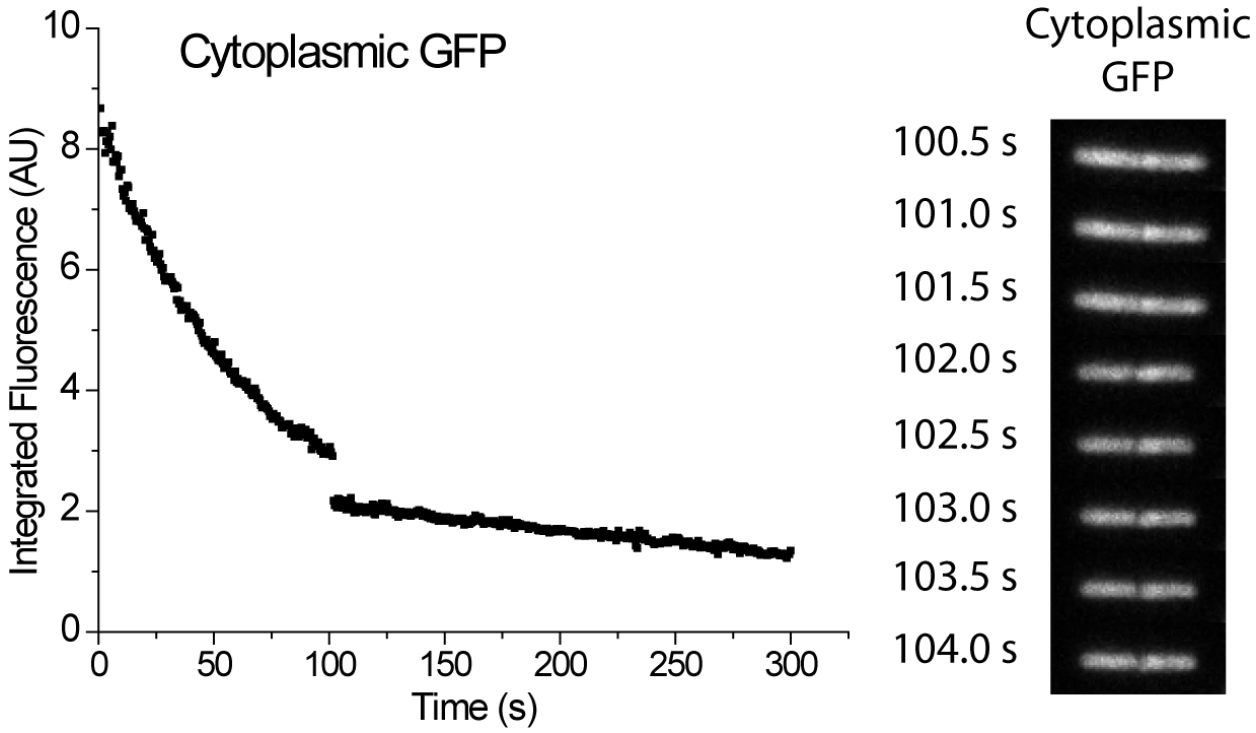

Figure 2E.1 Decrease in cytoplasmic GFP fluorescence intensity after cell shrinkage. Integrated intensity vs. time (left) shows that there is a ~25% drop in fluorescence intensity at t = 102 s, which corresponds to the moment of cell shrinkage as shown in the images (right). Injection of LL-37 occurred ~1 min before the start of data acquisition. The gradual decrease in fluorescence intensity, most noticeable in the first 100 s, is due to photobleaching.

Appendix 2F: Time to Capture for Diffusion of Molecules in a Sphere

A simple model problem enables us to estimate the time required for cytoplasmic GFP to exit a pore in the membrane. A sphere of radius *R* is uniformly filled with particles diffusing with coefficient *D.* The surface of the sphere has a perfectly absorbing circular patch of radius *b*, mimicking the pore. The mean time to capture $\bar{W}$ is given approximately by

(Eq. 24, [40]):

$$\bar{W} \approx 4R^2/3D\theta_c \quad \theta_c \leq 0.1 \text{ radians} \qquad \text{Eq. (2F.1)}$$

Here $\theta_c = b/R$. To mimic the *B. subtilis* cytoplasm, we take R = 1.06 μm, making the volume of the sphere 5 μm^3 (which is somewhat smaller than the typical volume of our *B. subtilis* cells). An assumed pore radius of 3 nm gives θ_c = 0.00283. Assuming a diffusion constant of D_{GFP} = 15 $\mu m^2/s$, the mean capture time becomes $\bar{W}$ = 35 s.

The fast movies of GFP fluorescence taken during cell shrinkage after exposure to LL-37 showed that the abrupt 20-30% decrease in GFP intensity occurs within 0.5 s, a factor of 70 faster than the estimate for $\bar{W}$. If we double the pore radius and double the diffusion coefficient, the model capture time is still 18 times longer than the upper limit from experiment. Moreover, we are comparing the complete time for the abrupt decrease with the mean time to capture from the model. We are also assuming that a GFP molecule that finds the patch is immediately lost to the cell surroundings, *i.e.*, the possibly slow transit time through the pore is neglected.

We therefore conclude that the abrupt loss of GFP intensity is not due to loss through a pore. Instead, we believe it is a photophysical process related to the change in pH induced by pore formation, as argued in the main text.

Appendix 2G: Effects of Nigericin on B. subtilis Producing Cytoplasmic GFP

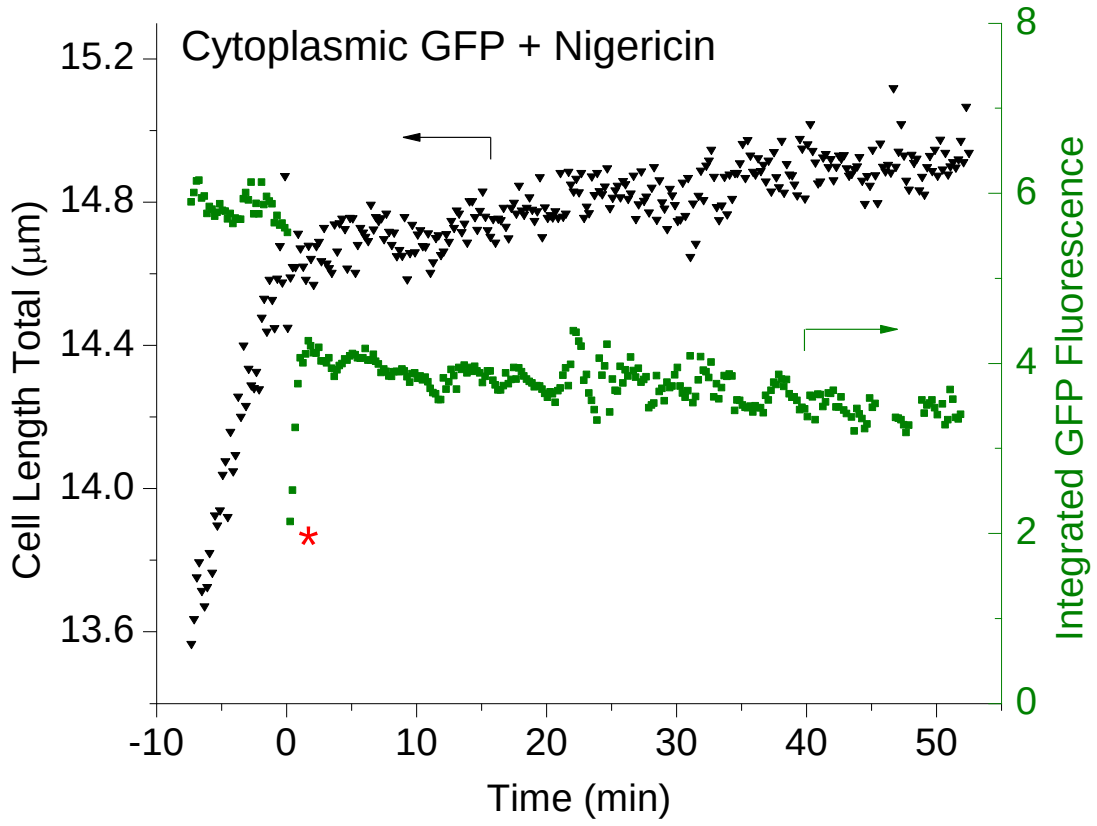

Figure 2G.1. Injection of 5 μM nigericin into flow chamber containing *B. subtilis* cells expressing cytoplasmic GFP. Injection of the nigericin solution occurred at time zero. The green squares (GFP fluorescence intensity) use the *y*-axis on the right. The black inverted triangles (length) use the *y*-axis on the left. The 30% decrease in total GFP intensity after the effects of nigericin is measured from the frames before injection, and the frames after the intensity has leveled off to its new plateau. We ignore the abrupt dip in GFP intensity marked by the red asterisk (*). The effect labeled by (*) may be due to pH re-equilibration after injection of nigericin, but we are not certain of this.]

References

1. **Brogden, K.A., *Antimicrobial peptides: pore formers or metabolic inhibitors in bacteria?* Nat Rev Microbiol, 2005. 3(3): p. 238-50.**

2. **Zasloff, M., *Antimicrobial peptides of multicellular organisms.* Nature, 2002. 415(6870): p. 389-95.**

3. **Wimley, W.C. and K. Hristova, *Antimicrobial peptides: successes, challenges and unanswered questions.* J Membr Biol, 2011. 239(1-2): p. 27-34.**

4. **Melo, M.N., R. Ferre, and M.A. Castanho, *Antimicrobial peptides: linking partition, activity and high membrane-bound concentrations.* Nat Rev Microbiol, 2009. 7(3): p. 245-50.**

5. **Andrews, J.M., *Determination of minimum inhibitory concentrations.* J Antimicrob Chemother, 2001. 48 Suppl 1: p. 5-16.**

6. **Scocchi, M., A. Tossi, and R. Gennaro, *Proline-rich antimicrobial peptides: converging to a non-lytic mechanism of action.* Cell Mol Life Sci, 2011. 68(13): p. 2317-30.**

7. **Schneider, T., et al., *Plectasin, a fungal defensin, targets the bacterial cell wall precursor Lipid II.* Science, 2010. 328(5982): p. 1168-72.**

8. **Pietiainen, M., et al., *Cationic antimicrobial peptides elicit a complex stress response in Bacillus subtilis that involves ECF-type sigma factors and two-component signal transduction systems.* Microbiology, 2005. 151(Pt 5): p. 1577-92.**

9. **Huang, H.W., F.Y. Chen, and M.T. Lee, *Molecular mechanism of Peptide-induced pores in membranes.* Phys Rev Lett, 2004. 92(19): p. 198304.**

10. **Epand, R.M. and R.F. Epand, *Bacterial membrane lipids in the action of antimicrobial agents.* J Pept Sci, 2011. 17(5): p. 298-305.**

11. **Shai, Y., *Mode of action of membrane active antimicrobial peptides.* Biopolymers, 2002. 66(4): p. 236-48.**

12. **Oren, Z., et al., *Structure and organization of the human antimicrobial peptide LL-37 in phospholipid membranes: relevance to the molecular basis for its non-cell-selective activity.* Biochem J, 1999. 341 (Pt 3): p. 501-13.**

13. **Porcelli, F., et al., *NMR structure of the cathelicidin-derived human antimicrobial peptide LL-37 in dodecylphosphocholine micelles.* Biochemistry, 2008. 47(20): p. 5565-72.**

14. **Lee, C.C., et al., *Transmembrane pores formed by human antimicrobial peptide LL-37.* Biophys J, 2011. 100(7): p. 1688-96.**

15. **Henzler Wildman, K.A., D.K. Lee, and A. Ramamoorthy, *Mechanism of lipid bilayer disruption by the human antimicrobial peptide, LL-37.* Biochemistry, 2003. 42(21): p. 6545-58.**

16. **Sengupta, D., et al., *Toroidal pores formed by antimicrobial peptides show significant disorder.* Biochim Biophys Acta, 2008. 1778(10): p. 2308-17.**

17. **Leontiadou, H., A.E. Mark, and S.J. Marrink, *Antimicrobial peptides in action.* J Am Chem Soc, 2006. 128(37): p. 12156-61.**

18. **Sochacki, K.A., et al., *Real-time attack on single Escherichia coli cells by the human antimicrobial peptide LL-37.* Proc Natl Acad Sci U S A, 2011. 108(16): p. E77-81.**

19. **Dunn, A.K. and J. Handelsman, *A vector for promoter trapping in Bacillus cereus.* Gene, 1999. 226(2): p. 297-305.**

20. **Cutting, S.M. and C.R. Harwood, eds. *Molecular Biological Methods for Bacillus*. 1990, John Wiley & Sons.**

21. **Nakano, M.M., et al., *Characterization of anaerobic fermentative growth of Bacillus subtilis: identification of fermentation end products and genes required for growth.* J Bacteriol, 1997. 179(21): p. 6749-55.**

22. **Rasband, W.S. *ImageJ*. 1997; http://rsb.info.nih.gov/ij/:[http://rsb.info.nih.gov/ij/].**

23. **Sliusarenko, O., et al., *High-throughput, subpixel precision analysis of bacterial morphogenesis and intracellular spatio-temporal dynamics.* Mol Microbiol, 2011. 80(3): p. 612-27.**

24. **Roth, B.L., et al., *Bacterial viability and antibiotic susceptibility testing with SYTOX green nucleic acid stain.* Appl Environ Microbiol, 1997. 63(6): p. 2421-31.**

25. **Briandet, R., et al., *Fluorescence correlation spectroscopy to study diffusion and reaction of bacteriophages inside biofilms.* Appl Environ Microbiol, 2008. 74(7): p. 2135-43.**

26. **Elowitz, M.B., et al., *Protein mobility in the cytoplasm of Escherichia coli.* J Bacteriol, 1999. 181(1): p. 197-203.**

27. **Konopka, M.C., et al., *Crowding and confinement effects on protein diffusion in vivo.* J Bacteriol, 2006. 188(17): p. 6115-23.**

28. **Martinez, K.A., 2nd, et al., *Cytoplasmic pH response to acid stress in individual cells of Escherichia coli and Bacillus subtilis observed by fluorescence ratio imaging microscopy.* Appl Environ Microbiol, 2012. 78(10): p. 3706-14.**

29. **Breeuwer, P., et al., *A Novel Method for Continuous Determination of the Intracellular pH in Bacteria with the Internally Conjugated Fluorescent Probe 5 (and 6-)-Carboxyfluorescein Succinimidyl Ester.* Appl Environ Microbiol, 1996. 62(1): p. 178-83.**

30. **Kitko, R.D., et al., *Cytoplasmic acidification and the benzoate transcriptome in Bacillus subtilis.* PLoS One, 2009. 4(12): p. e8255.**

31. **Henderson, P.J., J.D. McGivan, and J.B. Chappell, *The action of certain antibiotics on mitochondrial, erythrocyte and artificial phospholipid membranes. The role of induced proton permeability.* Biochem J, 1969. 111(4): p. 521-35.**

32. **Lamsa, A., et al., *The Bacillus subtilis cannibalism toxin SDP collapses the proton motive force and induces autolysis.* Mol Microbiol, 2012. 84(3): p. 486-500.**

33. **Schuwirth, B.S., et al., *Structures of the bacterial ribosome at 3.5 A resolution.* Science, 2005. 310(5749): p. 827-34.**

34. **Demchick, P. and A.L. Koch, *The permeability of the wall fabric of Escherichia coli and Bacillus subtilis.* J Bacteriol, 1996. 178(3): p. 768-73.**

35. **Smith, T.J., S.A. Blackman, and S.J. Foster, *Autolysins of Bacillus subtilis: multiple enzymes with multiple functions.* Microbiology, 2000. 146 (Pt 2): p. 249-62.**

36. **Vollmer, W., et al., *Bacterial peptidoglycan (murein) hydrolases.* FEMS Microbiol Rev, 2008. 32(2): p. 259-86.**

37. **Sochacki, K.A., in *Chemistry*. 2011, University of Wisconsin-Madison: Madison, WI.**

38. **Huang, H.W., *Molecular mechanism of antimicrobial peptides: the origin of cooperativity.* Biochim Biophys Acta, 2006. 1758(9): p. 1292-302.**

39. **Jacobs-Wagner, C. *MicrobeTracker Suite*. 2011; http://microbetracker.org/help/helpMicrobeTrackerOutput.htm:[**

40. **Linderman, J.J. and D.A. Lauffenburger, *Analysis of intracellular receptor/ligand sorting. Calculation of mean surface and bulk diffusion times within a sphere.* Biophys J, 1986. 50(2): p. 295-305.**

Chapter 3

Real Time Attack of Alamethicin on Single *B. subtilis* Cells

Introduction

Alamethicin (ALM) was discovered in the late 1960's, produced by the fungus *Trichoderma viride*, and has been used as a model pore-forming peptide for decades. [1, 2] Alamethicin has a unique primary sequence, highlighted by non-standard amino acids, and unique C- and N- terminal modifications. The primary sequence for ALM F50 is [3]: AcU-P-U*-A*-U*-A*-Q-U-V*-U-G-L*-U-P-V*-U-U*-Q-Q-Fol. Alamethicin F50 has glutamine (Q) at position 18, while alamethicin F30 has glutamic acid (E). U is α-methylalanine, AcU is acetylated α-methylalanine, and Fol is phenylalaninol. An asterisk next to an amino acid indicates there is heterogeneity in the actual residue at that location; alamethicin does not have a single sequence. ALM has activity against Gram-positive bacteria but not Gram-negative, making it an excellent candidate for study with *B. subtilis*.

Alamethicin can make amphipathic helices [4], like LL-37, but the details of its membrane disruption are quite different. Alamethicin is one of the few AMP's that can make barrel-stave pores in model lipid bilayers. [5, 6] This likens the peptide to a "channel-former", which is consistent with conductance data taken on model lipid bilayers exposed to alamethicin. [7] However, data on the mycoplasma *Spiroplasma melliferum* shows that dissipation of membrane potential is followed by lysis, suggesting that the formation of small pores may not fully describe its antimicrobial action. [8]

We present data of alamethicin acting on *B. subtilis*. We are able to obtain constant flow conditions in these experiments, which gives us a greater degree of control of the effective peptide concentration in the flow chamber. Our data shows interesting similarities and differences between LL-37 and alamethicin, and that the formation of small, barrel-stave pores may not explain all of the symptoms of alamethicin exposure.

Materials and Methods

Chemicals

The water used for all experiments was ultrapure water (>18 MΩ) from a Millipore Simplicity 185 filter system. Alamethicin was purchased from Sigma-Aldrich (>98%, Catalog no. A4665) and dissolved in ethanol to a concentration of 5 mg/mL. Alamethicin from Sigma-Aldrich is predominately the F50 form, with trace amounts of the F30 form. LL-37 was purchased from Anaspec (95% pure, Catalog no. 61302, Fremont, CA) and dissolved in water to make a 1 mM stock solution A 5 mM Sytox Orange solution in DMSO was purchased from Molecular Probes (Catalog no. S11368). A 5 μM working solution of Sytox Orange was made in water. The sodium salt of nigericin was purchased from Sigma Aldrich (≥98%, Catalog no. N7143) and dissolved in ethanol. Chicken egg-white lysozyme was purchased from Sigma-Aldrich (Catalog no. L4919, Bioultra) and dissolved in water. Supplements used for the media (5X EZ supplement Beta, M3104; 10X ACGU Beta, M3103; 10X MOPS mix, M2137) were purchased from Teknova.

Strains and Growth Conditions

B. subtilis 168 from the Bacillus Genetic Stock Center (BGSC, code 1A1) was used as the wild type strain. Our strain producing cytoplasmic GFP is *B. subtilis* 168 transformed with plasmid pAD43-25 and was used previously (Chapter 2). Most experiments used the cytoplasmic GFP producing *B. subtilis* strain. The strain with pAD43-25 was grown with 5 μg/mL chloroamphenicol to select for the plasmid. Chloroamphenical was omitted when imaging the strain. All strains were grown in *subtilis*-EZRDM at 37 °C and 200 rpm (0.9 g) in a New Brunswick Excella E24 Incubator-Shaker. Cultures were grown in *s*-EZRDM overnight, inoculated from a frozen glycerol culture. The following day, dilutions of at least 1/200 were made into pre-warmed *s*-EZRDM. Cells were grown to an OD of 0.04–0.06 (600 nm, 1 mm path length) as measured on a Nanodrop 2000 from Thermo Scientific, and then harvested for microscopy or MIC measurements.

Minimum Inhibitory Concentration (MIC) Assay

MICs were measured only on wild type *B. subtilis*. A serial dilution of alamethicin was performed in one row of a polystyrene 96-well plate in *s*-EZRDM, beginning at 128 μg/mL and with twofold dilution at each step. The final volume in each well in the row was 50 μL after serial dilution. A liquid cell culture was grown in the same conditions as described in "Strains and Growth Conditions," to a final OD of 0.04–0.06. This culture was diluted in *s*-EZRDM to an OD of 0.005. 50 μL of the diluted culture was added to each well of the alamethicin serial dilution, so that the maximum concentration tested was 64 μg/mL. The final OD in each well was 0.0025, and the final volume in each well was 100 μL. A second row contained 50 μL of *s*-EZRDM plus 50 μL of inoculum (positive growth control), while a third row contained 100 μL of *s*-EZRDM in each well (negative growth control and blank for OD measurements). The plate was incubated at 37 °C while shaking at 200 rpm (0.9 g) in an Excella 24 Incubator/Shaker from New Brunswick Scientific for 6 hours. The "6-hr MIC" is reported as the lowest concentration for which no cell growth could be detected after 6 hr, as determined by measurements of OD at 595 nm using a Wallac EnVision 2100 Multilabel Reader from Perkin–Elmer. The MIC experiments were performed three times, and were reproducible to within a dilution factor of two. The 6-hr MIC for alamethicin was 16 μg/mL. We cannot report an exact molar concentration of alamethicin, since alamethicin from Sigma Aldrich and other companies is a mixture of different isoforms. Assuming an approximate molecular weight of 2 kDa, 16 μg/mL of alamethicin is ~ 8 μM.

Microscopy Experiments

The home built, temperature-controlled flow chamber, with an internal volume of ~60 μL (3 X 31 X 0.75 mm), was described previously [9], with the modification to coverslip preparation described in Ref [10]. The fully assembled flow chamber was placed in a vacuum chamber for 1-5 min, to help remove unwanted bubbles trapped in the chamber. The flow chamber was then placed onto the microscope setup,

and allowed to equilibrate to 37 °C. Cells harvested from the mid-log phase liquid culture were injected into the flow chamber, and rinsed with at least 0.8 mL of fresh medium to remove unadhered cells.

Our previous study [10] using LL-37 was performed without constant flow, meaning that after the LL-37 solution was injected into the flow chamber, the medium was static. Partially due to the lower cost of alamethicin, we were able to constantly flow alamethicin throughout the experiment, using syringe pumps (model NE-300) from SyringePump.com. Most experiments were performed as follows. After the cells were injected into the flow chamber and rinsed with medium, the chamber was attached to two syringe pumps through tubing connected by a y-junction from Warner Instruments. A picture of the setup is given in Appendix A. *s*-EZRDM was flowed at a rate of 0.1 mL/min for the first 7 min of the data acquisition, at which point the flow was changed to a separate syringe containing alamethicin and 2 nM Sytox Orange. Sytox Orange is a "dead-cell stain" similar to Sytox Green (at low enough concentrations, it will only stain cells that have a compromised membrane), except that it has a different excitation/emission spectrum (547/570 nm). The use of Sytox Orange allows us to carry out two-color imaging of cytoplasmic GFP and DNA staining in the same cell. The initial injection of alamethicin/Sytox Orange in *s*-EZRDM was performed at 2 mL/min for 30 seconds, to fully rinse the cells with the growth medium containing alamethicin/Sytox Orange. The flow of the alamethicin/Sytox Orange solution in growth medium was then changed to 0.1 mL/min for the rest of the data acquisition, to conserve the consumption of alamethicin. The average doubling time for the cytoplasmic GFP producing *B. subtilis* cells in the first 7 min period was 44±5 min (±standard deviation of 19 cells), based on tip-to-tip measurements of cell length vs time. Experiments with different injection parameters will be noted in the text.

Using our constant flow setup, we are able to maintain the concentration of alamethicin in the chamber to a higher degree of accuracy than before. In particular, using constant flow, we are able to see major symptoms of antimicrobial stress at 1X the MIC (6-h MIC is16 μg/mL for alamethicin) in less than one hour after injection, whereas to see major symptoms for LL-37 without flow at the same time scale,

concentrations 2-4X the MIC were required (6-h MIC for LL-37 was 1 μM [10]). When we perform our experiments from the previous study using LL-37 and the constant flow setup, the major symptoms of antimicrobial stress appear at lower concentrations (1-2X the 6-h MIC) than with the static flow chamber. We believe that the higher concentrations required in our previous study were caused by the effective concentration of LL-37 being reduced, due to adherence of the peptide to components in the chamber.

Microscopy movies were taken on a Nikon Eclipse TE300 microscope, equipped with a Nikon Phase Contrast Type DLL Objective, NA=1.3. All filters were from Chroma Technology. A 500 nm long-pass filter (HQ500LP) was used in the microscope dichroic cube. Three different channels were imaged; cytoplasmic GFP (using the 488 line from an Ar^+ laser, and an ET525/50 emission filter), Sytox Orange (using a 561 nm Sapphire laser from Coherent, and a HQ600/50M emission filter), and phase contrast (using the HQ600/50M filter). Images were taken with an Andor Ixon 897 EMCCD camera.

Time lapse movies were taken as follows. An image with 488nm excitation was taken first, then an image with 561nm excitation, then a phase contrast image. These images were taken 6 sec apart, at 50 ms exposure times. This gives a cycle time of 18 sec. This cycle was repeated 300 times to get an hour long movie. Growth medium alone was flowed during the first 70 frames of the movie. At frame 70, the flow was switched to growth medium containing alamethicin and Sytox Orange. The fast movies imaging the fluorescence of Sytox Orange only were taken with a 0.5 sec cycle time.

Data Analysis

Movies from time-lapse imaging were analyzed using imageJ [11],and the program microbeTracker [12], using algorithm 4 with modifications to the following parameters: areaMin = 300, thresFactorM = 1.2, thresFactorF = 1.2, splitThreshold =2, joindist = 8, joinangle = 1.2. Cells were selected for full analysis based on how well they stayed in focus during the movie, and if they were separated enough from other cells to allow integrated intensities to be measured. MicrobeTracker calculates the tip-to-tip cell length, as well as the cell volume, assuming that the cell is symmetric around its short axis. Analysis of *B. subtilis* cells was performed the same as it was for our LL-37 experiments.

Results

Symptoms of Antimicrobial Stress at 1X MIC: Cell Length and Sytox Orange Staining

While 19 cells were fully analyzed for this study, we first describe in detail the effects of alamethicin on two example cells of *B. subtilis*. Figure 3.1 shows results for a single *B. subtilis* cell (Fig. 3.1A) and a double cell (Fig 3.1B) exposed to 16 μg/mL alamethicin (1X MIC). A double cell (or doublet) is two *Bacillus subtilis* cells that have evidently undergone membrane septation (and thus, have separate cytoplasms), but are still connected by their peptidoglycan layers. This septal region for *B. subtilis* can be very small (< 300 nm, [13]), and cannot be resolved by phase contrast microscopy until the cells have separated further. Based on observations of cell shrinkage events and the Sytox Orange staining pattern, the majority of the cells in our study are doublets. We review the symptoms of alamethicin stress on a single *B. subtilis* cell to illustrate the details of our analysis, and then review a double cell as more representative of our data set.

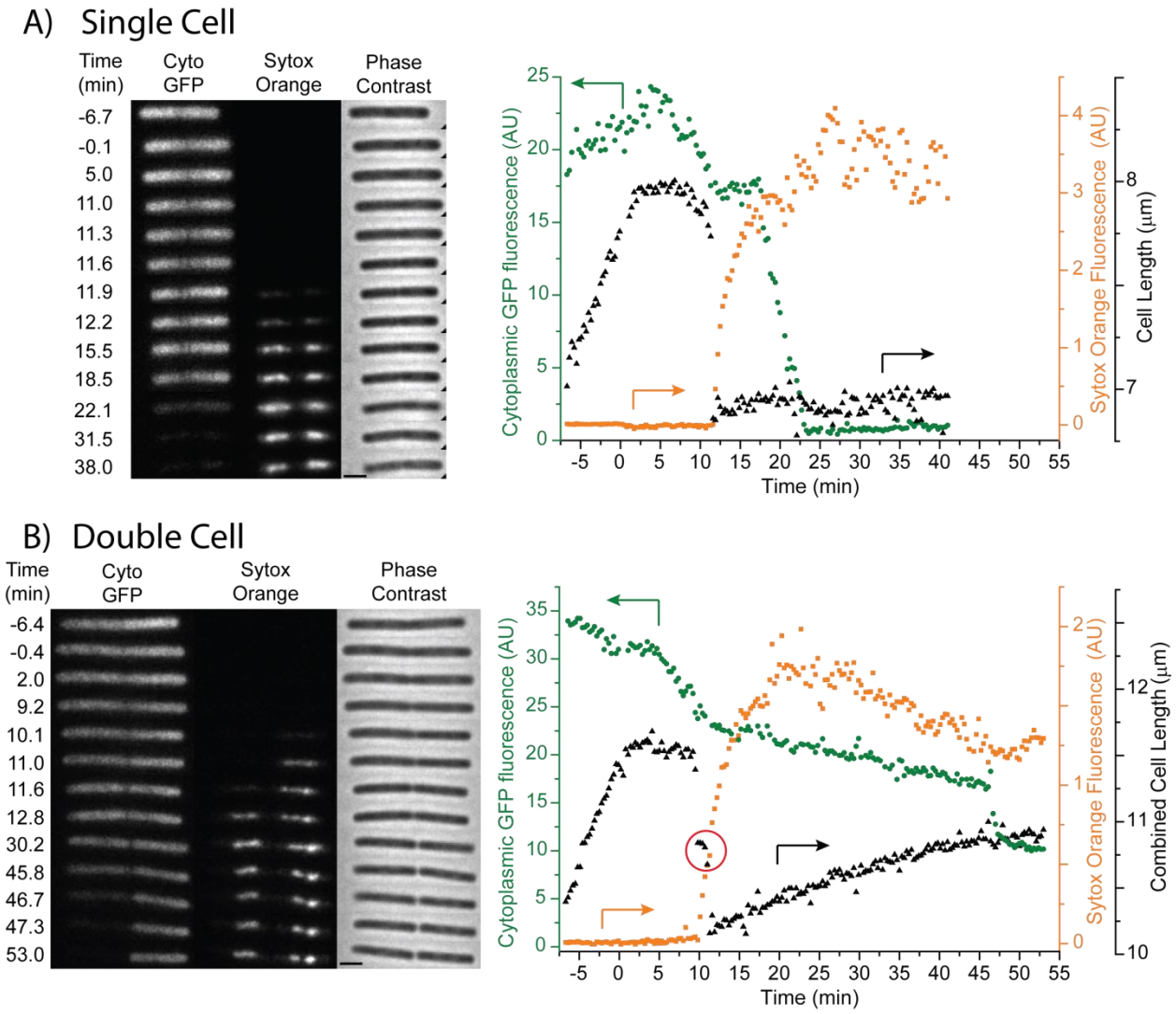

Figure 3.1 Images and analysis for A) a single *B. subtilis* cell, and B) two *B. subtilis* cells (double cell), exposed to 16 μg/mL alamethicin (1X MIC) and 2 nM Sytox Orange. Injection of the alamethicin/Sytox Orange solution began at time zero. Green circles denote the integrated intensity of cytoplasmic GFP, orange squares are for the integrated intensity of Sytox Orange, and black triangles are for cell length. The colored arrows point to the respective y axes. The red circled region in B) highlights the time between the 1st and 2nd shrinkage events. Scale bar is 2 μm.

Alamethicin is injected at $t = 0$. In Fig. 3.1A, cell length plateaus within 3 min of injection of alamethicin, suggesting the cessation of growth. The cell then exhibits a gradual decrease in cell length that occurs 9 to 11 min after injection of alamethicin, followed by a large and abrupt decrease in cell length between 11.3 and 11.6 min. Cell length does not change after this large decrease in cell length,

which we call abrupt shrinkage. Staining of the nucleoid with Sytox Orange begins within one frame (18 sec) of the abrupt shrinkage event; there is no evidence of staining at earlier times. Sytox Orange will only stain the nucleoids of cells with compromised membrane integrity. There is no data on the cell after t = 40 min due to a bubble rinsing away the cells during the experiment. Interpretation of the cytoplasmic GFP integrated intensity is more complex, and will be discussed later in the text.

Figure 3.1B shows analysis of a *B. subtilis* doublet. The combined cell length of the doublet plateaus within 3 min of alamethicin injection, as it did for the single cell in Fig. 3.1A. Subsequently, there are two large, abrupt decreases in cell length, between 9.2 and 9.8 min, and between 10.7 and 11.3 min. The values of cell length in between these abrupt shrinkage events are highlighted by a red circle in the figure. We interpret the two shrinkages as one cell of the doublet shrinking, followed by the other cell shrinking, confirming that a septum has formed. In Fig. 3.1B, the cell on the right shrinks first, followed by the cell on the left. This is supported by the phase contrast images at t = 10.1 and 11.6 min, as well as the images of nucleoid staining by Sytox Orange. Sytox Orange stains the cell on the right first, and then stains the cell on the left. If the cytoplasms of the two cells were still connected, we would expect cell shrinkage and Sytox Orange staining to occur simultaneously. Evidence of a septal region can be seen as early as t = 10.1 min, and the septum is clearly seen by t = 30.2 min. For all cells studied, the average time between injection of alamethicin and the conclusion of all abrupt shrinkage events is 10.9 ± 2.3 min (± standard deviation of 19 cells).

After abrupt shrinkage is over, cell length increases for the doublet (Fig 3.1B), but not the single cell (Fig 3.1A). All other cells studied exhibited increases in cell length after abrupt cell shrinkage. As argued in our previous study on LL-37 (Chapter 2), we do not believe that this is actual cell growth, but instead are changes in cell length and width that preserve cell volume. In all 19 cells studied, cell volume (as calculated by MicrobeTracker) did not increase after shrinkage. Examples are given in Appendix 3B. We utilize cell length instead of cell volume in our analysis because it is less sensitive to the cells going out of focus in the microscope.

Symptoms of Antimicrobial Stress at 1X the MIC: Cytoplasmic GFP

The cytoplasmic GFP intensity curves we present here show 3 distinct "phases." Each phase shows a decrease in cytoplasmic GFP integrated intensity, but the cause of this decrease differs for one of the 3 phases. To begin, we will review the behaviors in cytoplasmic GFP integrated intensity for the cells in Fig. 3.1. We will then consider the average integrated intensity of all 19 cells studied, which will allow us to draw a picture of the 3 different phases of GFP integrated intensity decrease.

For the single cell in Fig. 3.1A, there are two decreases in GFP integrated intensity. The first begins at 5.3 min and ends once the cell has shrunk. We do not think this decrease in intensity is due to GFP leakage, because the cell does not exhibit staining by the much smaller Sytox Orange. The decrease between 5.3 min and cell shrinkage correlates in time with the plateau of cell length. As with our results with cytoplasmic GFP and LL-37 (Chapter 2), we believe this decrease in GFP intensity is due to a decrease in intracellular pH. Our hypothesis is that alamethicin is causing pH equilibration between the cytoplasm (pH ~7.8-8.1, [14, 15]) and the buffered growth medium (pH = 7.4). The reduction in cytoplasmic pH will cause a reduction in GFP fluorescence, which agrees with our experimental trends and other studies on cytoplasmic GFP in *B. subtilis*. [16] The dissipation of ΔpH across the membrane should affect cell growth, which is seen in the plateauing of cell length in Fig. 3.1A. The first reduction in GFP fluorescence ends at the same time the cell becomes permeabilized to Sytox Orange. This interpretation is consistent with the formation of small, barrel-stave pores permeable to protons. Alamethicin has been shown to form small pores in model lipid bilayers. [5, 6]

In Fig. 3.1A, there is a second decrease in GFP intensity that begins at 17.6 min and ends at 23.3 min. The integrated intensity is nearly zero after this second decrease. We believe this decrease in GFP intensity is due to delayed leakage of GFP from the cytoplasm of *B. subtilis*. This interpretation is supported by the images of cytoplasmic GFP in Fig. 3.1A, which show no visible GFP signal by 31.5 min. This loss of GFP occurs well after both the abrupt shrinkage event and Sytox Orange staining,

suggesting that the cell membrane is becoming permeable to larger species as time goes by. This is similar to results of LL-37 on *B. subtilis* that express GFP. (Chapter 2)

The double cell in Figure 3.1B also displays a decrease in GFP intensity, again beginning at $t = 5$ min and ending once both members of the doublet have shrunk. The decrease again correlates with the plateau in cell length, and Sytox Orange has not yet stained the nucleoid. We assign this as another example of pH equilibration across the cytoplasmic membrane. There is then a second, more gradual decrease in GFP integrated intensity between the abrupt cell shrinkage event and continuing to $t = 46.4$ min. This gradual decrease occurs simultaneously for both cells in the doublet, as determined by the integrated intensities of the individual cells as a function of time (data not shown). From $t = 46.4$ to 48.5 min, there is a large and abrupt drop in GFP integrated intensity. This is due to the left cell in the doublet abruptly leaking its remaining cytoplasmic GFP. The right cell does not exhibit full loss of GFP during the time scale of the experiment. The gradual decrease in integrated intensity between shrinkage and 46.4 min is apparently due to gradual leakage of cytoplasmic GFP. The sudden loss of GFP from the left cell at 48.5 min represents a sudden increase in the permeability of the diffusion barrier keeping GFP inside the cell. Whether this diffusion barrier is the membrane or the peptidoglycan layer will be addressed below.

To summarize, there are 3 distinct "phases" in GFP integrated intensity in the cells in Figure. 3.1. The first phase, occurring in the 5 min prior to cell shrinkage, we attribute to equilibration of ΔpH across the membrane. The second phase, present in the doublet in Fig. 3.1B between 11.3 and 46.4 min, we call a *gradual* decrease in GFP intensity. The third phase, starting at 17.6 min for the single cell in Fig. 3.1A and 46.4 min for the doublet in Fig. 3.1B, we call an *abrupt* decrease in GFP intensity. We define an abrupt decrease in GFP intensity by the following criteria. First, the beginning of an abrupt GFP intensity decrease is marked by a change in the slope of the GFP intensity decrease, as shown at 17.6 min for the single cell in Fig. 3.1A, and at 46.4 min for the doublet in Fig. 3.1B. Second, this abrupt decrease should result in the loss of all intracellular cytoplasmic GFP intensity.

While these 3 phases can be seen in Fig. 3.1, the integrated intensity curves for GFP are still noisy. The single cell in Fig. 3.1A shows an increase in integrated intensity prior to injection of alamethicin, and the doublet in Fig. 3.1B shows a decrease. To confirm our interpretations of the 3 "phases" of GFP intensity, we took the average of the integrated intensity curves for all 19 cells. This is shown in Fig. 3.2, with the average represented as a thick green line, and the curves of individual cells shown in gray. The integrated intensity of each cell was normalized to one to place them on the same scale. Since each cell undergoes symptoms at a different timescale, Fig. 3.2 uses a new t' time scale with $t' = 0$ defined as the time at which the last abrupt shrinkage event had finished.

For the data in Fig. 3.2, only the data prior to an *abrupt* decrease in GFP intensity was included. The abrupt decreases in GFP intensity are excluded in Fig. 3.2 because they occur at variable times after cell shrinkage, and would greatly skew the average. Appendix 3C gives examples of a few of the integrated intensity curves that are included in Fig. 3.2, and denotes what data points from those curves were excluded due to abrupt GFP intensity decreases.

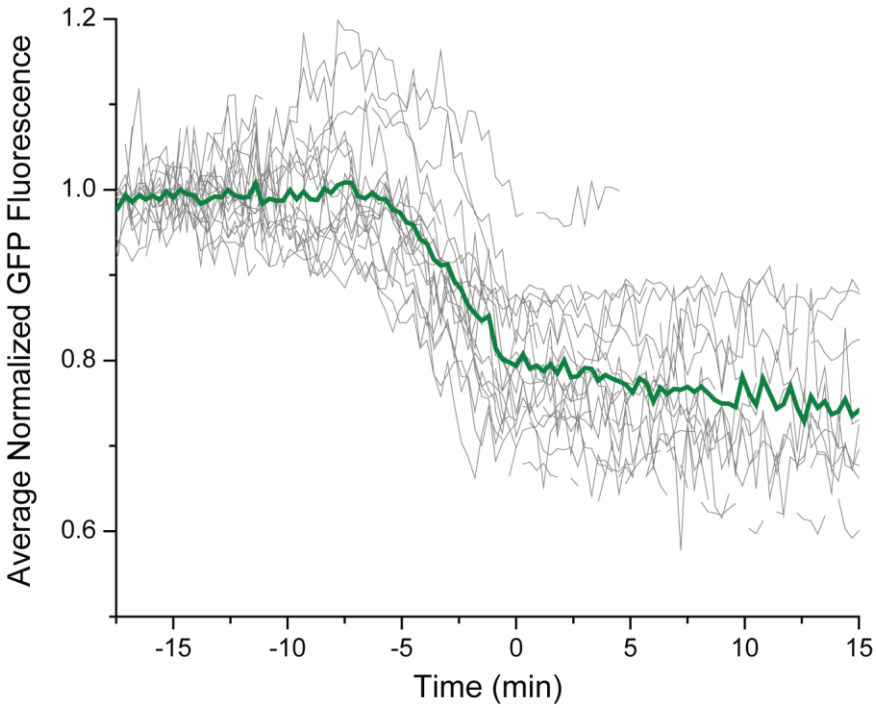

Figure 3.2 Average normalized GFP integrated intensities for 19 cells exposed to 16 µg/mL alamethicin. Individual cell plots are shown in gray; the average of the 19 cells is the thick green line. Each cell has time zero set as the time at which all cell shrinkage events have finished. The time of alamethicin injection varies from –17.1 to –7.5 min. The average decrease in GFP intensity is 20%, as measured from the plateau prior to shrinkage and the value of the integrated intensity immediately after shrinkage.

The average normalized GFP intensity prior to *t*' = -7.5 min includes the time before injection of alamethicin. On average, this intensity is flat. This indicates that photobleaching of GFP is unimportant on the time scale of Fig. 3.2. In contrast, in Fig. 3.1 the intensity prior to injection of alamethicin was either increasing (Fig. 3.1A) or decreasing (Fig. 3.1B). The average behavior of Fig. 3.2 suggests that such intensity changes prior to injection are due to noise and do not reflect actual changes in cytoplasmic GFP fluorescence.

Returning to Fig. 3.2, between t' = -7.5 and the time of cell shrinkage (t' = 0) there is a real decrease in average GFP intensity by ~20%. As described above, we believe the decrease in GFP

intensity that occurs immediately prior to shrinkage is due to pH equilibration across the cytoplasmic membrane, consistent with the formation of pores. This will be corroborated below using nigericin to equilibrate pH across the cytoplasmic membrane. Between t' = 0 and 15 min, there is a second real decrease in the average GFP intensity by an additional 10%. This is similar to the gradual decrease in GFP intensity we saw for the double cell in Fig. 3.1B. The majority of the 19 cells studied showed this gradual decrease in GFP intensity, which occurs after cell shrinkage, but prior to an abrupt decrease in GFP intensity (examples are given in Appendix 3A). Because pH has already equilibrated, this gradual decrease is evidently due to real leakage of GFP from the cytoplasm. The abrupt intensity decreases are due to an increase in the rate of GFP leakage, most likely caused by an increase in the permeability of the diffusion barrier (being either the membrane or the peptidoglycan layer).

To confirm that the first decrease in GFP intensity (prior to cell shrinkage) is due to a decrease in intracellular pH, we used nigericin as a positive control. Nigericin is an ionophore that we used in our LL-37 study to remove the ΔpH across the cellular membrane. If the decrease in GFP intensity is due to a reduction in intracellular pH, cells treated with nigericin first, then alamethicin, will not show a second decrease in GFP intensity after injection of alamethicin. This data is shown in Figure 3.3. The injection of nigericin at t = 0 causes an abrupt ~30% decrease in GFP intensity, but alamethicin exposure at 16 μg/mL 6 min after nigericin exposure causes no additional change in GFP intensity, even for those cells that shrink during the movie. This supports the idea that the initial reduction of GFP intensity is due to the dissipation of ΔpH, *i.e.*, to a reduction in intracellular pH, and not to real loss of GFP from the cytoplasm.

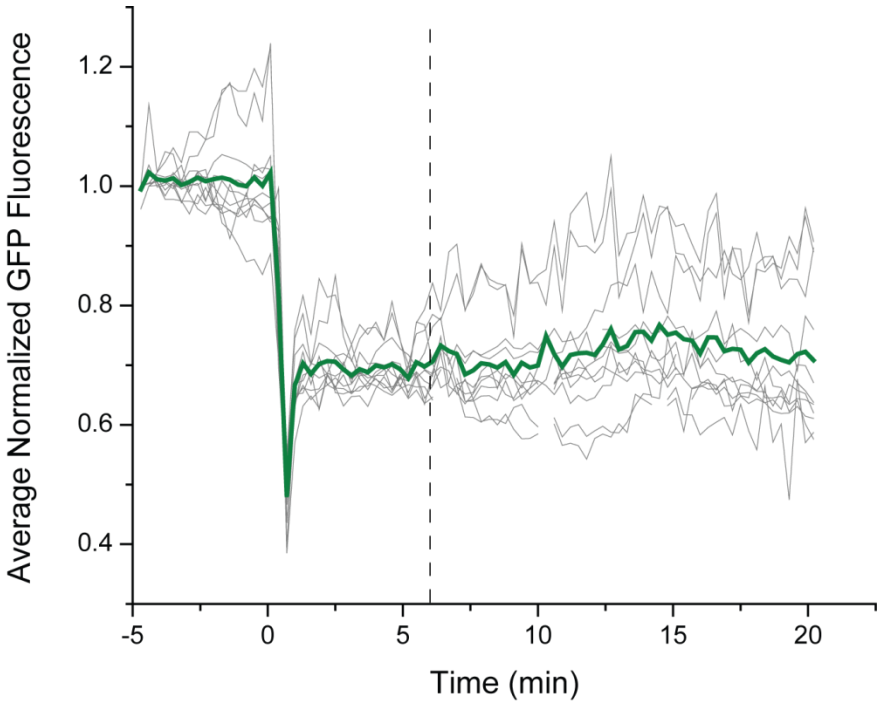

Figure 3.3 Average normalized GFP fluorescence for 11 cells exposed to nigericin, then alamethicin. 5 µM nigericin solution was injected at time zero, while 5 µM nigericin/16 µg/mL alamethicin solution was injected at time 6 min (dashed line). Syringe A contained alamethicin/nigercin in *s*-EZRDM, while Syringe B contained only nigericin in *s*-EZRDM. Growth medium was not being flowed before the injection of nigericin at time zero. All 11 cells exhibit cell shrinkage and Sytox Orange staining between t = 6 min until the end of data acquisition. Pretreatment with nigericin at 0 min causes no significant change in GFP integrated intensity after injection of alamethicin/nigericin at 6 min. The drop in GFP intensity from the initial plateau until the new plateau around 0 min is ~30%.

What is the Barrier to GFP Efflux?

As shown in Fig. 3.1 and 3.2, after cell shrinkage and DNA staining by Sytox Orange, GFP exhibits two kinds of decreases in intensity; *gradual* decreases in GFP intensity, and *abrupt* decreases. We interpret both of these decreases as actual losses of GFP from the cytoplasm. For certain, cytoplasmic GFP is not exiting the cytoplasm at the same time as cell shrinkage and nucleoid staining by Sytox

Orange (or for cell shrinkage and nucleoid staining by Sytox Green for our LL-37 results). In our experiments on *E. coli* and LL-37 [9], the cytoplasmic membrane becomes permeable to Sytox Green (1 kDa) and GFP (27 kDa) at the same time. This suggests that in *B. subtilis*, there is still a barrier to GFP effusion after cell shrinkage. What is the effusion barrier for cytoplasmic GFP in *B. subtilis*: the cytoplasmic membrane, or the peptidoglycan layer?

Autolysins are enzymes that degrade the peptidoglycan layer, necessary for insertion of new glycan strands and for cell separation. [17, 18] After cell shrinkage and the onset of Sytox Orange staining, there should be no more peptidoglycan synthesis due to the loss of the proton motive force and of intracellular ATP. (ATP is much smaller than Sytox Orange, and should quickly leak out of the cytoplasm.) However, when peptidoglycan synthesis has stopped, the autolysins are still enzymatically degrading the peptidoglycan layer, a reaction that occurs outside the cytoplasm and does not require an energized membrane. [19] Our hypothesis is that after permeabilization of the cytoplasmic membrane to Sytox Orange, GFP cannot initially permeate through the shrunken peptidoglycan layer. The autolysins gradually degrade the peptidoglycan layer, causing the delayed loss of GFP. Once it begins, GFP loss seemingly occurs at a rate that varies widely from cell to cell. The same cell can exhibit both gradual leakage (t = 11.3 to 46.4 min for the double cell in Fig. 3.1B) and abrupt leakage (t = 46.4 to 48.5 min for Fig. 3.1B) of cytoplasmic GFP. If the autolysin hypothesis is correct, then any agent that increases the rate of peptidoglycan degradation would decrease the time delay between shrinkage and abrupt GFP leakage.

We designed an experiment to test this theory, using lysozyme to increase the rate of peptidoglycan degradation. Lysozyme hydrolyzes the bond between the two sugars in the saccharide chain, N-acetylmuramic acid and N-acetylglucosamine. The experiment used the same imaging cycle as before; only the flow conditions were changed. *B. subtilis* cells were inside the flow chamber, under static conditions (no flow), for the first 2 min of data acquisition. A 16 µg/mL alamethicin/2 nM Sytox Orange solution in growth medium was injected at a rate of 2 mL/min for 30 sec. The flow was then

changed to 0.1 mL/min. After all of the cells had shrunk (10 min into the movie), a solution of 0.2 μg/mL lysozyme/2 nM Sytox Orange was injected into the flow chamber at a rate of 2 mL/min for 1 min. The flow was then changed to 0.1 mL/min for the remainder of the movie. (We are unable to flow growth medium prior to injection of alamethicin, since it would require a third syringe pump.)

The time lag between shrinkage and loss of GFP (Δt) is defined as $\Delta t = t_{GFP} - t_{shrink}$, where t_{shrink} is the time of cell shrinkage, and t_{GFP} is the time of *abrupt* GFP loss. For the cell in Fig. 3.1A, Δt = 17.3 – 11.6 = 5.7 min. For the double cell in Fig. 3.1B, Δt = 46.4 – 11.3 = 35.1 min. The distribution of Δt values for cells exposed to lysozyme after addition of alamethicin is compared to the experiments performed after addition of alamethicin alone in Fig. 3.4. The histogram for the experiments without lysozyme comes from the same data set described above. However, the number of useful cells for the main analysis was only 19 due to the requirement that cells remain well adhered throughout the long imaging period. For the histogram in Fig. 3.4, we only need to note the time of shrinkage and the time of abrupt GFP loss. This increases our data set to N = 68 for cells without lysozyme, and N = 22 for cells exposed to lysozyme.

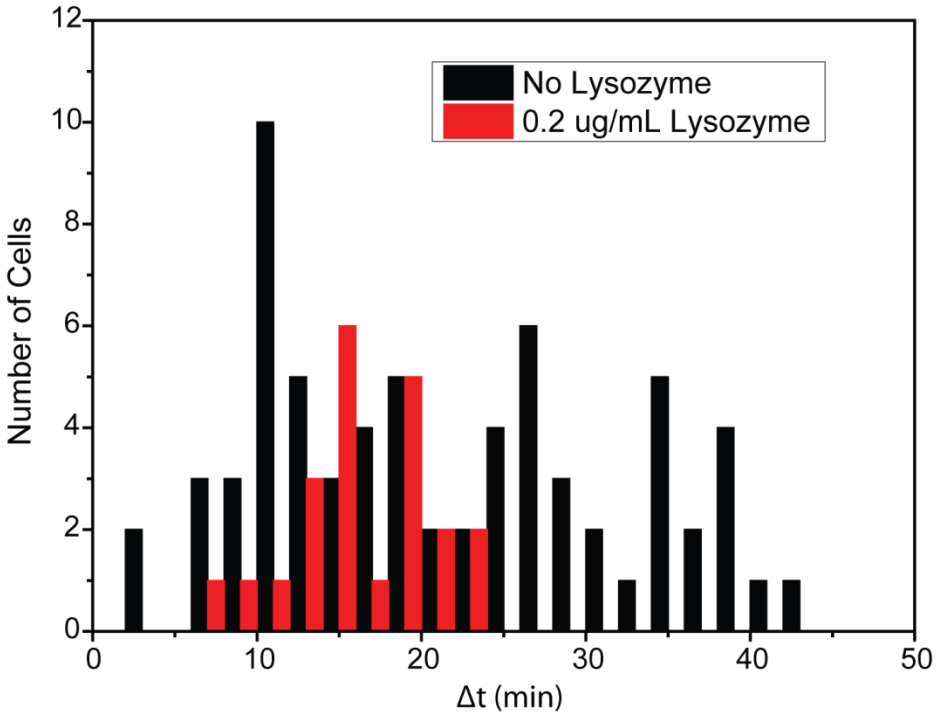

Figure 3.4 Distribution of Δt ($\Delta t = t_{GFP\ loss} - t_{shrink}$) for cells exposed to 16 µg/mL alamethicin, with lysozyme (red bars) and without (black bars) lysozyme. The lysozyme concentration used was 0.2 µg/mL.

Figure 3.4 shows a significant shift in the distribution of Δt values to shorter times when cells are exposed to lysozyme after shrinkage, consistent with the hypothesis that the peptidoglycan layer is the main diffusion barrier to GFP efflux. Application of the same 0.2 µg/mL of lysozyme alone to *B. subtilis* cells does not cause loss of GFP or shrinkage on an hour long time scale (data not shown). The data shown here are preliminary; the experimental conditions for the lysozyme experiments are not identical to the conditions for cells exposed to only alamethicin. In the lysozyme experiments, the cells are in a static flow chamber prior to alamethicin exposure, in contrast to a constant flow of growth medium present in the experiments without lysozyme. Also, cells in the lysozyme experiment were only exposed to alamethicin for a brief period (<10 min) to allow cells to shrink. The experiments without lysozyme exposed cells to alamethicin for the entire experiment. Additional experiments will be performed to ensure that these experimental conditions do not account for the shift in distribution of Δt in Fig. 3.4.

Non-Localized Staining of the B. subtilis Nucleoid

In our previous study on LL-37, Sytox Green stained the nucleoid in a non-uniform way after shrinkage. Sytox Green would initially stain only a small portion of the nucleoid, and then the staining would spread out to cover the rest of the nucleoid. These observations indicate a localized membrane disruption, which only allows Sytox Green to enter at a specific location of the cell envelope. There is the question as to whether or not alamethicin, an antimicrobial peptide from a different organism than LL-37, also leads to localized membrane permeabilization. Our previous study used Sytox Green instead of Sytox Orange, and the growth medium was static after injection of LL-37. To enable a better comparison with the present alamethicin study, we carried out a constant flow experiment using LL-37 at 2X its MIC and Sytox Orange to stain the nucleoids. The LL-37 and alamethicin experiments also used the same data acquisition parameters (0.5 sec/frame, only Sytox Orange was imaged).

Figure 3.5 shows the nucleoid staining dynamics of *B. subtilis* cells exposed to 2 μM LL-37 or 16 μg/mL alamethicin (both 1X the MIC). Injection of alamethicin or LL-37 occurred prior to the start of the movie, due to the lag time between injection and cell shrinkage, and the fast imaging rate. The exact time of cell shrinkage is unknown, since we cannot simultaneously image the Sytox Orange channel and phase contrast while taking images at 0.5 sec/frame. As shown in Fig. 3.5, cells exposed to LL-37 again display initially localized Sytox Orange staining that spreads to the entire nucleoid on a ~1 min timescale. In sharp contrast, alamethicin causes uniform staining of the nucleoid on a sub-minute timescale.

Although LL-37 and alamethicin both cause simultaneous membrane permeabilization, cell shrinkage, and Sytox Orange staining of the nucleoids, the initial permeabilization is localized for LL-37 and global for alamethicin. This strongly suggests substantial mechanistic differences at the molecular level. Perhaps alamethicin induces many widely distributed pores essentially simultaneously throughout

the membrane. Alternatively, the results suggest the possibility of a global, carpet-like permeabilization mechanism. We discuss these possibilities in more detail below.

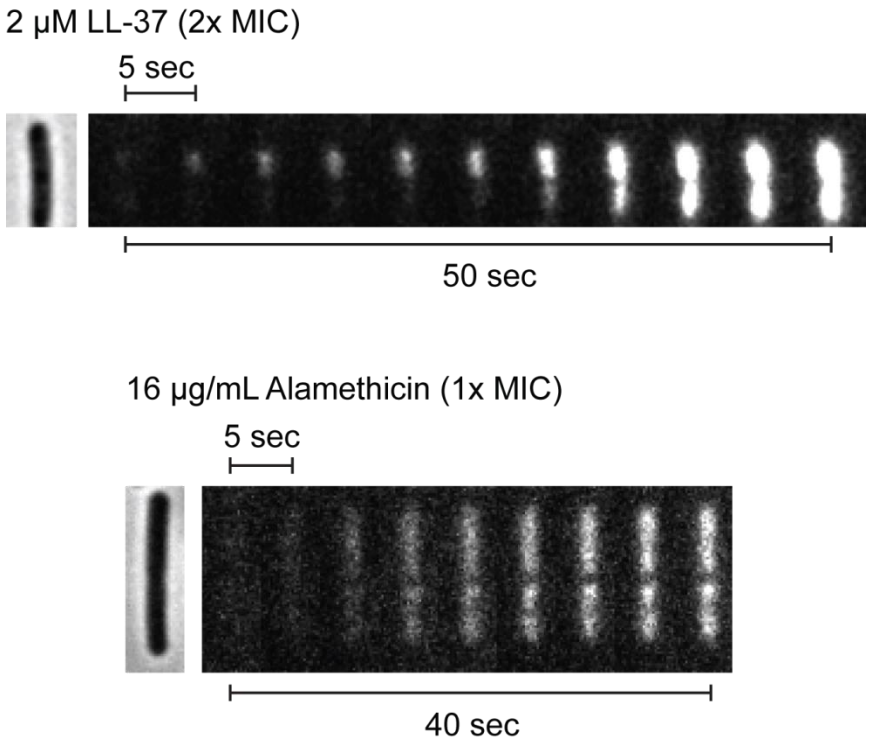

Figure 3.5 Sytox Orange staining dynamics of cells exposed to 2 µM LL-37 (2X MIC), or 16 µg/mL alamethicin (1X MIC). Only the Sytox Orange was imaged as a function of time. One phase contrast image was taken before the start of the Sytox Orange data acquisition. Data were taken at 0.5 sec/frame. Only every 10^{th} frame is shown due to the timescale of nucleoid staining. The exact time of cell shrinkage is unknown, since we could not take phase contrast images while simultaneously imaging the Sytox Orange channel at 0.5 sec/frame.

Long Term Effects of Alamethicin Exposure

Our analysis has focused on the symptoms of alamethicin exposure on an hour-long time scale. We attempted to observe the effects of alamethicin on *B. subtilis* at longer time scales and to determine if shrinkage is recoverable by rinsing alamethicin away with fresh growth medium. Unfortunately, cells that have shrunk due to alamethicin action tend to detach from the coverslip, which severely hinders our

ability to observe cells for longer time periods. We do observe a few cells losing phase contrast on a time scale of 2 to 4 hr, much as observed at long times after treatment with LL-37. An example is given in Fig. 3.6. This indicates permeabilization of the cell envelope to the chromosomal DNA, ribosomes, and other large cytoplasmic species. The "ghost-like" remaining images indicate that a remnant of the cell envelope remains, *i.e.*, the entire envelope is not solubilized (as might occur with detergent).

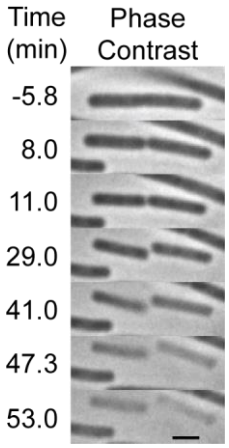

Figure 3.6 Example of cell losing phase contrast ~40 min after injection of alamethicin. Time zero is the time of injection of alamethicin. Cell shrinkage occurs between 8 and 11 min. Loss of phase contrast occurs from 41 to 53 min, which is the end of data acquisition. The cell was stained with Sytox Orange after shrinkage, and lost cytoplasmic GFP before 41 min (data not shown). This cell is not one of the 19 cells studied for the main analysis.

Discussion

Cells exposed to LL-37 or alamethicin show important differences prior to cell shrinkage. While the alamethicin and LL-37 experiments were taken under different growth conditions, we still believe there are meaningful comparisons to be made. At 4 μM LL-37, cells shrink within 4 min of exposure to the AMP. There are no obvious symptoms before cell shrinkage; cell growth continues up until the moment of shrinkage. This is in contrast to alamethicin, which causes noticeable symptoms prior to shrinkage, including the halting of cell growth (as measured by cell length) and the dissipation of ΔpH (as measured by cytoplasmic GFP intensity). At 2 μM LL-37, cell shrinkage is not observed on an hour long

time scale, even though growth rate is attenuated. *B. subtilis* exposed to alamethicin at 0.5X MIC (data not shown) still led to cell shrinkage, even though there was a longer delay between injection and cell shrinkage. The fact that LL-37 does not show noticeable symptoms prior to cell shrinkage may be due to its tendency to oligomerize. [20] Oligomers of LL-37 may require time to unbundle before they interact with the bacterial membrane. The time delay between alamethicin introduction and symptoms appears to be determined by the lag time to form membrane pores.

The most striking difference between LL-37 and alamethicin may be occurring at the molecular level. The localized Sytox Orange staining found with LL-37 is in stark contrast to the "global" staining of cells exposed to alamethicin. While the exact structure of the LL-37 lipid disruption is unknown, it is unlikely that it is making the well-defined barrel-stave pores found with alamethicin. Even though alamethicin has been shown to form a structured pore in lipid bilayers, the disruption that leads to shrinkage and Sytox Orange staining in real cells is not occurring at a localized position on the lipid membrane. This suggests that alamethicin is not forming a single pore that eventually becomes larger, but is creating several pores that are all increasing in size.

Experiments on model lipid bilayers estimate the inner diameter of the alamethicin pore to be between 1.8 and 2.6 nm, depending on the type of lipid used. [5] Alamethicin can also equilibrate monovalent cations across bilayers. [7] Assuming Sytox Orange has the same hydrodynamic radius as Sytox Green (1 nm, [21]), it is possible for Sytox Orange to pass through a pore of this size. Since we do not see Sytox Orange staining while the ΔpH is being dissipated, this suggests that alamethicin, at least initially, is not forming pores of this size. Since the cell eventually releases larger species like GFP, the disruption in the membrane becomes larger at longer times of alamethicin exposure. This suggests that alamethicin forming small, barrel-stave pores is not the final step in its antimicrobial action. Barrel-stave pores are transitioning into larger membrane disruptions, and autolysins may be playing a role in eventual cell death as evidenced by cell lysis shown in Fig. 3.6.

While our lysozyme experiments do not prove that the PG layer is the diffusion barrier to GFP leakage, the data is consistent with this interpretation. The porosity of the PG layer in *B. subtilis* has an estimated maximum mass cutoff of ~50 kDa. [22] 50 kDa is the maximum for stretched sacculi. GFP is a 27 kDa protein, so it is possible that the PG layer is the diffusion barrier for unstretched saculli (as is the case when cells have shrunk). The reason that the PG layer could be a diffusion barrier for GFP in *B. subtilis* but not *E. coli* may not be due to a difference in the inherent size of the pores in the PG layer, but due to the difference in the number of PG layers. Since *B. subtilis* can have a PG layer between 15 to 30 nm, compared to E. coli's 1.5-15 nm [23], the main diffusion barrier could be caused by the GFP having to find another "hole" in the next PG layer, after having found the first one. It should be stated that elucidating the exact three-dimensional structure of the entire Gram-positive PG layer is still an active area of research.

Since there is evidence of membrane potential disruption, there is the question as to why we have not used membrane potential dyes. $DiOC_2$ has been used before on *Bacillus subtilis*. [24] Unfortunately, the dyes themselves are toxic to cells. Exposure of bacteria to 30 µM DiOC2 results in the death of 99% of the cells after only 4 min. [25] Imaging of the dye itself can lead to cell perturbations (unpublished observations). While GFP is a more benign ΔpH sensor, there are improvements that could be made in the method. Placing GFP on an inducible promoter to control expression, and the use of a GFP variant more sensitive to changes in pH (such as pHluorin), could result in more stable GFP signals from individual cells.

Our results show similarities to one of the few in-depth studies of alamethicin acting on bacteria. This study showed an initial loss of membrane potential, followed by eventual cell lysis, of the mycoplasma *Spiroplasma melliferum*. [8] Mycoplasma are bacteria that do not have a peptidoglycan layer. To determine what role, if any, the PG layer has in the interaction of alamethicin with *B. subtilis*, studying cell wall-less forms of *B. subtilis* (L-forms, [26]) would provide an interesting comparison to the mycoplasma results.

Appendix 3A: Constant Flow Setup for Alamethicin Experiments

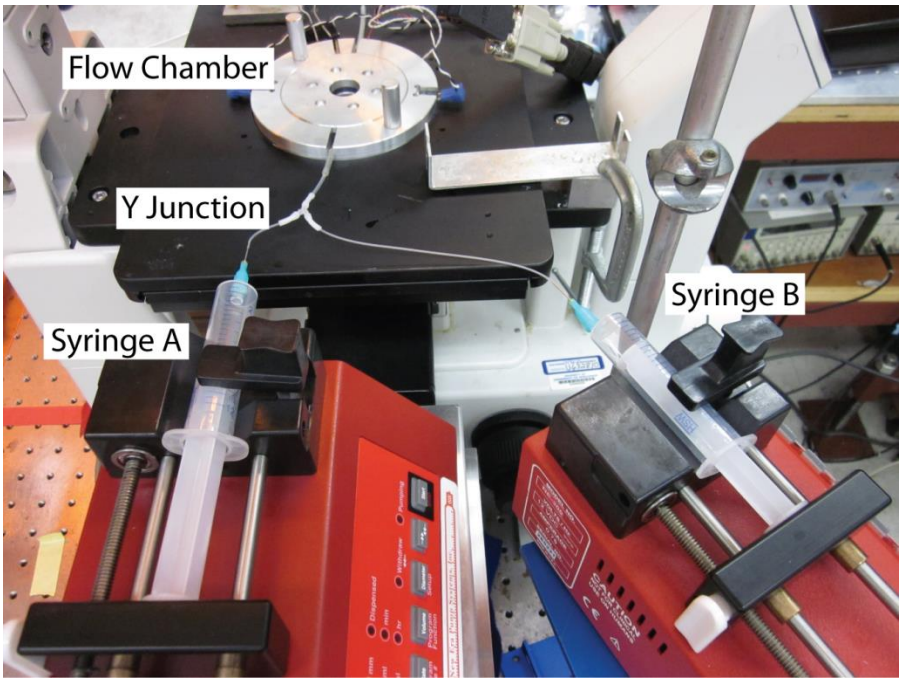

Figure 3A.1 The flow chamber setup has two syringes connected by a y-junction that leads to the flow chamber. Syringe A typically contained the alamethicin/Sytox Orange/*s*-EZRDM solution, and Syringe B contained only *s*-EZRDM, unless otherwise stated in the text. To ensure that alamethicin was not being flowed into the chamber due to diffusion at the y-junction, the tubing before the y-junction was filled with *s*-EZRDM only.

Appendix 3B: Cell Volume and Length

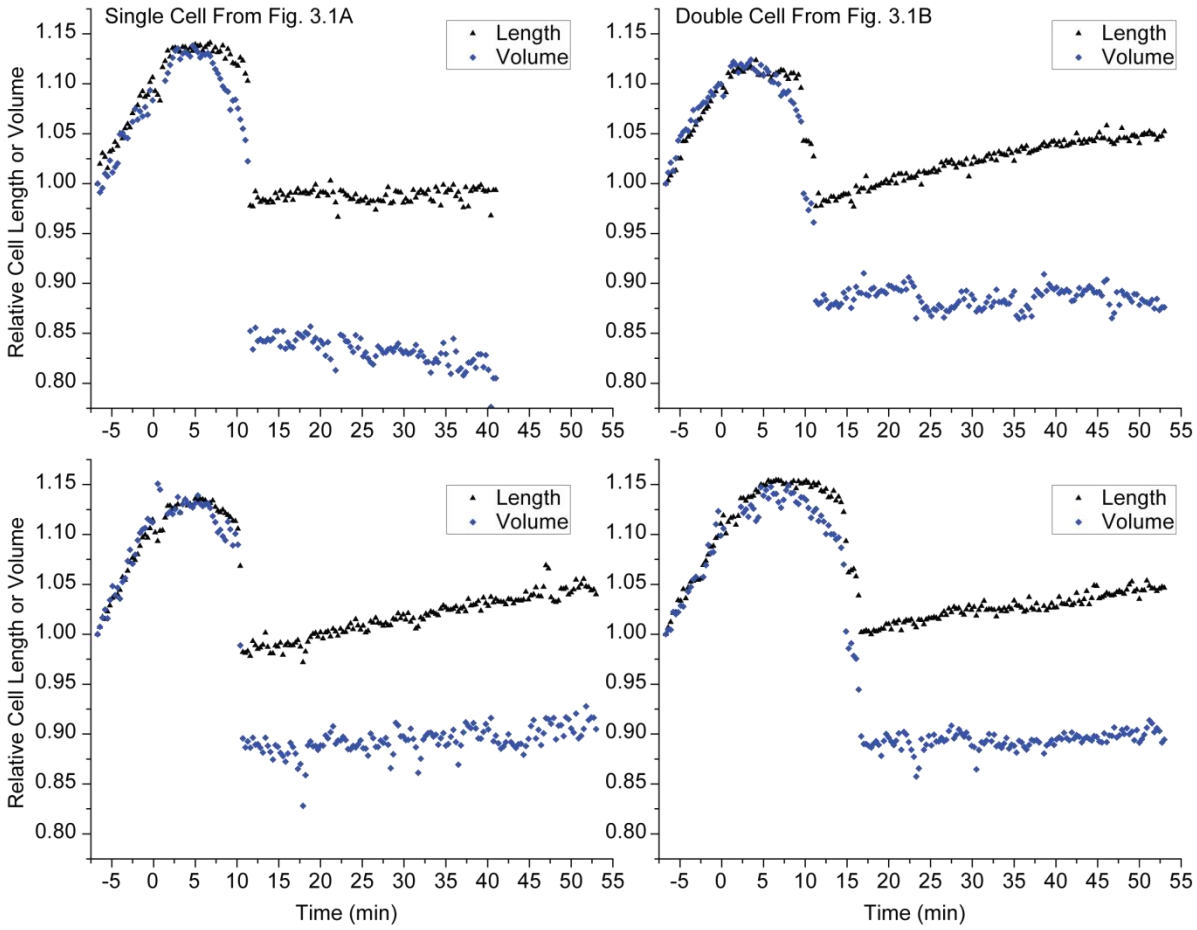

Figure 3B.1 Plots of relative cell length (black triangles) and relative cell volume (blue diamonds) during exposure to 16 µg/mL alamethicin. Time zero is the time of injection of the alamethicin solution. The lengths and volumes were normalized to one to show the curves on the same y-axis, and for ease of comparison. The plots at top left and top right are for the cells in Fig. 3.1A and Fig. 3.1B, respectively. The plots at the bottom are for 2 additional sample cells. Each cell in the figure is from a different experimental run.

Appendix 3C: Integrated Intensity Curves of Cytoplasmic GFP in *B. subtilis*

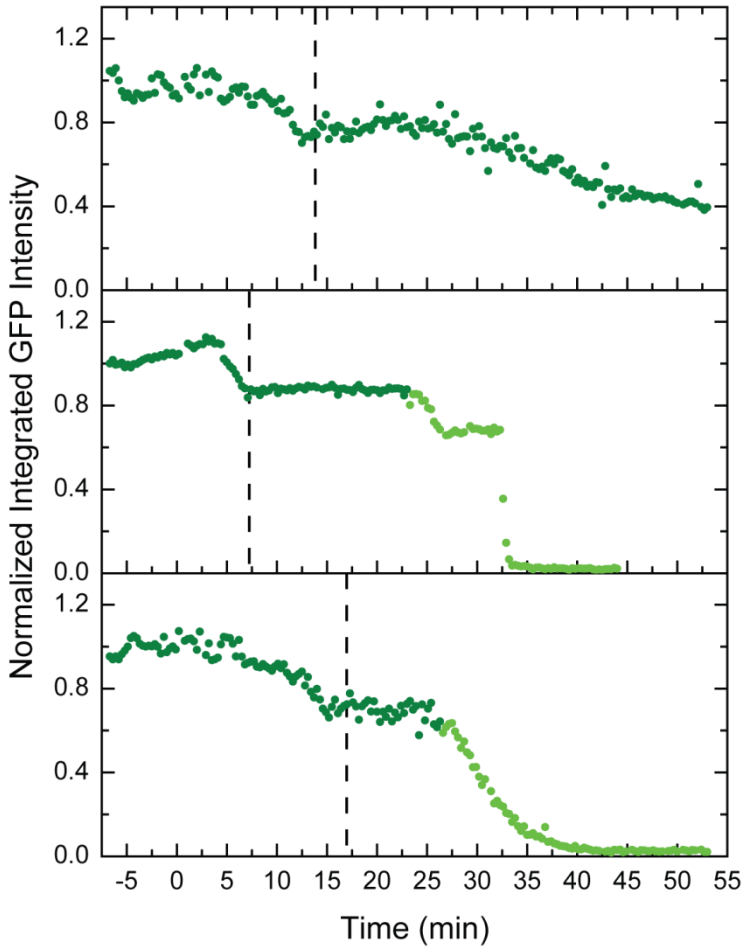

Figure 3C.1 Normalized GFP integrated intensity curves for 3 sample *B. subtilis* cells. For this graph, $t = 0$ is the time of alamethicin injection. The dashed lines mark the time of cell shrinkage. The dark green circles are data that were included in the average integrated GFP intensity plot (Fig. 3.2). The light green circles are data that were excluded from the average intensity plot, due to abrupt decreases in GFP intensity as defined in the main text. Note that for the bottom graph, the loss of cytoplasmic GFP at $t = 27.5$ min continues for over ~ 10 min; this is still called an abrupt decrease in GFP intensity, due to the sudden change in slope, as well as the complete loss of cytoplasmic GFP at the end (the integrated intensity is 0).

References

1. **Leitgeb, B., et al., *The history of alamethicin: a review of the most extensively studied peptaibol.* Chemistry & biodiversity, 2007. 4(6): p. 1027-51.**

2. **Kredics, L., et al., *Recent results in alamethicin research.* Chemistry & biodiversity, 2013. 10(5): p. 744-71.**

3. **Kirschbaum, J., et al., *Sequences of alamethicins F30 and F50 reconsidered and reconciled.* Journal of peptide science : an official publication of the European Peptide Society, 2003. 9(11-12): p. 799-809.**

4. **Fox, R.O., Jr. and F.M. Richards, *A voltage-gated ion channel model inferred from the crystal structure of alamethicin at 1.5-A resolution.* Nature, 1982. 300(5890): p. 325-30.**

5. **He, K., et al., *Neutron scattering in the plane of membranes: structure of alamethicin pores.* Biophysical journal, 1996. 70(6): p. 2659-66.**

6. **Qian, S., et al., *Structure of the alamethicin pore reconstructed by x-ray diffraction analysis.* Biophysical journal, 2008. 94(9): p. 3512-22.**

7. **Duclohier, H. and H. Wroblewski, *Voltage-dependent pore formation and antimicrobial activity by alamethicin and analogues.* The Journal of membrane biology, 2001. 184(1): p. 1-12.**

8. **Beven, L., et al., *Correlation between anti-bacterial activity and pore sizes of two classes of voltage-dependent channel-forming peptides.* Biochimica et biophysica acta, 1999. 1421(1): p. 53-63.**

9. **Sochacki, K.A., et al., *Real-time attack on single Escherichia coli cells by the human antimicrobial peptide LL-37.* Proc Natl Acad Sci U S A, 2011. 108(16): p. E77-81.**

10. **Barns, K.J. and J.C. Weisshaar, *Real-time attack of LL-37 on single Bacillus subtilis cells.* Biochim Biophys Acta, 2013. 1828(6): p. 1511-20.**

11. **Rasband, W.S. *ImageJ*. 1997; http://rsb.info.nih.gov/ij/:[http://rsb.info.nih.gov/ij/].**

12. **Jacobs-Wagner, C. *MicrobeTracker Suite*. 2011; http://microbetracker.org/help/helpMicrobeTrackerOutput.htm:[**

13. **Birdsell, D.C., R.J. Doyle, and M. Morgenstern, *Organization of teichoic acid in the cell wall of Bacillus subtilis.* Journal of bacteriology, 1975. 121(2): p. 726-34.**

14. **Martinez, K.A., 2nd, et al., *Cytoplasmic pH response to acid stress in individual cells of Escherichia coli and Bacillus subtilis observed by fluorescence ratio imaging microscopy.* Appl Environ Microbiol, 2012. 78(10): p. 3706-14.**

15. **Breeuwer, P., et al., *A Novel Method for Continuous Determination of the Intracellular pH in Bacteria with the Internally Conjugated Fluorescent Probe 5 (and 6-)-Carboxyfluorescein Succinimidyl Ester.* Appl Environ Microbiol, 1996. 62(1): p. 178-83.**

16. **Kitko, R.D., et al., *Cytoplasmic acidification and the benzoate transcriptome in Bacillus subtilis.* PLoS One, 2009. 4(12): p. e8255.**

17. **Smith, T.J., S.A. Blackman, and S.J. Foster, *Autolysins of Bacillus subtilis: multiple enzymes with multiple functions.* Microbiology, 2000. 146 (Pt 2): p. 249-62.**

18. **Vollmer, W., et al., *Bacterial peptidoglycan (murein) hydrolases.* FEMS Microbiol Rev, 2008. 32(2): p. 259-86.**

19. **Jolliffe, L.K., R.J. Doyle, and U.N. Streips, *The energized membrane and cellular autolysis in Bacillus subtilis.* Cell, 1981. 25(3): p. 753-63.**

20. **Oren, Z., et al., *Structure and organization of the human antimicrobial peptide LL-37 in phospholipid membranes: relevance to the molecular basis for its non-cell-selective activity.* Biochem J, 1999. 341 (Pt 3): p. 501-13.**

21. **Briandet, R., et al., *Fluorescence correlation spectroscopy to study diffusion and reaction of bacteriophages inside biofilms.* Appl Environ Microbiol, 2008. 74(7): p. 2135-43.**

22. **Demchick, P. and A.L. Koch, *The permeability of the wall fabric of Escherichia coli and Bacillus subtilis.* J Bacteriol, 1996. 178(3): p. 768-73.**

23. **Vollmer, W., D. Blanot, and M.A. de Pedro, *Peptidoglycan structure and architecture.* FEMS microbiology reviews, 2008. 32(2): p. 149-67.**

24. **Eun, Y.J., et al., *DCAP: a broad-spectrum antibiotic that targets the cytoplasmic membrane of bacteria.* Journal of the American Chemical Society, 2012. 134(28): p. 11322-5.**

25. **Novo, D., et al., *Accurate flow cytometric membrane potential measurement in bacteria using diethyloxacarbocyanine and a ratiometric technique.* Cytometry, 1999. 35(1): p. 55-63.**

26. **Leaver, M., et al., *Life without a wall or division machine in Bacillus subtilis.* Nature, 2009. 457(7231): p. 849-853.**